Received: 18 September 2025 | Revised: 20 March 2026 | Accepted: 31 March 2026

DOI: 10.1111/bph.70501

RESEARCH ARTICLE

Shared and specific molecular mechanisms of proteasome inhibitors in chemotherapy-induced peripheral neurotoxicity

Federico Iseppon[1] | Alessio Malacrida[1] | Alessia Chiorazzi[1] | Annalisa Canta[1] | Paola Alberti[1,2] | Valentina Alda Carozzi[1] | Eleonora Pozzi[1] | Virginia Rodriguez-Menendez[1] | Laura Cherchi[1] | Valentina Fabbro[1] | Lisa Pagani[3] | Elisa Tonelli[1] | Laura Tapella[4] | Andrea Mattarei[5] | Sara Palermo[6] | Daniele Cartelli[7] | Mario Mauri[8] | Noemi Scimia[9] | Serena Stanga[9] | Dmitry Lim[4] | Carla Distasi[4] | Marta Delconti[4] | Clizia Chinello[3] | Patricia Morcillo[10] | Maria Elena Pero[10,11] | Francesca Bartolini[10] | Guido Cavaletti[1,2] | Cristina Meregalli[1]

Correspondence
Cristina Meregalli, School of Medicine and Surgery, University of Milano-Bicocca, via Cadore 48, Monza, Monza and Brianza 20900, Italy.
Email: cristina.meregalli@unimib.it

Funding information
Ministero dell'Istruzione, dell'Università e della Ricerca, Grant/Award Number: P2022R43RA; Fondazione Cariplo, Grant/Award Number: 2019-1482; NIH/NCI, Grant/Award Number: R01CA279401A1; NIH/NIA, Grant/Award Number: RF1AG050658

Abstract

Background and Purpose: Proteasome inhibitors have been approved for treatment of multiple myeloma but induce significant chemotherapy-related peripheral neurotoxicity in up to one third of patients. Crucial information about the several neurotoxicity mechanisms suggested in the literature and effective triggering events is either missing or controversial, due to heterogeneity of experimental models used to investigate such processes. To fill this knowledge gap, we compared the neurotoxicity of bortezomib (BTZ) and carfilzomib (CFZ), a less neurotoxic drug, by investigating preclinical models and dissecting the underlying molecular mechanisms using a multidimensional approach.

Experimental Approach: We developed a new mouse model of CFZ-induced neuropathy and compared it with an established BTZ model using behavioural, morphological/morphometric and proteomic analyses of dorsal root ganglia (DRG) tissues. Mitotoxicity and cytoskeleton alterations were compared in terms of onset of altered mitochondrial morphology, functionality and trafficking, alongside cytoskeletal protein expression and axonal degeneration in cultured mouse DRG neurons.

Key Results: BTZ's severe neurotoxicity in vivo correlated with severe loss of nerve fibres and extensive protein expression changes. In vitro, both compounds significantly altered mitochondrial network organization and energy production after 24 h

Abbreviations: BIPN, bortezomib-induced peripheral neuropathy; BTZ, bortezomib; CFZ, carfilzomib; CIPN, chemotherapy-induced peripheral neuropathy; DAPI, 4′,6-diamidino-2-phenylindole; DRG, dorsal root ganglion; FDR, False Discovery Rate; IENF, intraepidermal nerve fibre; MAP, microtubule-associated protein; MiNA, Mitochondrial Network Analysis; MM, multiple myeloma; MTT, 3-(4,5-di methyl thiazol-2-yl)-2,5-diphenyltetrazolium bromide; OCR, oxygen consumption rate; PBMC, peripheral blood mononuclear cells; PFS, progression-free survival; OS, overall survival; RIPA, radio immunoprecipitation assay; RPMI, Roswell Park Memorial Institute; SAP, sensory action potential; SCV, sensory conduction velocity; VDAC, Voltage Dependent Anion Channel.

Federico Iseppon and Alessio Malacrida contributed equally.

For affiliations refer to page 23

of treatment. However, only BTZ induced accumulation of tubulin post-translational modifications and early axonal degeneration within the first 10 h, severely impacting mitochondrial trafficking after 24 h.

Conclusions and Implications: These results point to mitochondrial toxicity as a common downstream effect of both treatments, whereas BTZ-specific off-target activity on tubulin hyper-stability may initiate early mitochondrial trafficking alterations. This knowledge may inform future mitigation approaches.

KEYWORDS

axonal degeneration, bortezomib, carfilzomib, chemotherapy-induced peripheral neuropathy, mitochondria, mitochondrial trafficking, Δ2-tubulin

1 | INTRODUCTION

Chemotherapy-induced peripheral neurotoxicity (CIPN) is a common side effect of numerous chemotherapy treatments for cancer. It causes a degeneration that affects primarily the peripheral nerves at the extremities in a symmetrical, length-dependent distribution (Cavaletti et al., 2019; Yang, Zhao, et al., 2024).

Proteasome inhibitors are a class of chemotherapeutic agents developed for the treatment of liquid tumours and are particularly effective on multiple myeloma (MM), due to the reliance of these cells on proteasome function to degrade excess protein and survive: They offer much needed and tangible improvements in progression-free survival (PFS) and overall survival (OS), significantly decreasing the risk of death of 28% in patients in all different stages of multiple myeloma (MM) treatment (Wu et al., 2025; Yang, Yao, et al., 2024).

Bortezomib (BTZ) is a first-generation ubiquitin-proteasome system inhibitor approved by the Food and Drug Administration (FDA) in 2003 and used since then as a chemotherapeutic drug for the treatment of multiple myeloma. Inhibition of the proteasome results in perturbation of intracellular protein homeostasis by accumulation of the poly-ubiquitinated proteins, subsequently inducing cellular stress and apoptosis (Adams, 2004). Although BTZ treats multiple myeloma with high efficacy, the related peripheral neuropathy development in patients requires dose modification and changes in the treatment regimen (Peng et al., 2015). A second generation of proteasome inhibitors have been developed, including Carfilzomib (CFZ), an irreversible inhibitor that showed comparable and in some cases better performances and milder neurotoxicity and neuropathic symptoms in patients when compared with BTZ (Costa et al., 2024; Martin, 2013; Tan et al., 2023; Xie et al., 2022). However, treatment with CFZ, especially in combination with lenalidomide or dexamethasone, incurs the highest yearly treatment costs and presents a higher incidence for other types of adverse events, like cardiovascular toxicity, that need constant patient monitoring (Chen et al., 2017; Kumar et al., 2020; Roy et al., 2015; Xie et al., 2022). Therefore, further long-term studies are necessary to confirm its potential for clinical use. These differences in treatment costs, regimen and adverse effects, as well as the wide variety of patient medical profiles, call even more for the development of preclinical models to fully understand the molecular mechanisms underlying adverse effects of proteasome inhibitors and establish tailored therapeutic strategies that are not currently available in a clinical setting (Velasco et al., 2019; White et al., 2023). Because of its earlier discovery and approval in the clinic, BTZ and its neurotoxicity mechanisms have been under investigation for more than a decade, whereas there is still no pre-clinical model of CFZ-dependent neuropathy (Carozzi et al., 2013; Cavaletti et al., 2007; Meregalli et al., 2021).

The specific mechanisms underlying BTZ-dependent CIPN (BIPN), albeit extensively studied for many years, are yet to be fully understood. Recent research suggests that one of the major candidates for

What is already known

- Proteasome inhibitors cause significant peripheral neuropathy in one third of the patients.
- Bortezomib, unlike carfilzomib, can directly interact with and stabilize microtubules inducing axonal degeneration.

What does this study adds

- Both carfilzomib and bortezomib affect mitochondria structure, function and energy production.
- Bortezomib but not carfilzomib increases Δ2-tubulin levels inducing axon degeneration and impairment of mitochondrial motility.

What is the clinical significance

- Proteasome inhibitors present both shared and specific molecular mechanisms for peripheral neuropathy.
- Knowledge of specific effects of bortezomib allows for proactive toxicity management and future personalized therapies.

neurotoxicity is its off-target effect on microtubules, an event that may promote microtubule hyper-stability and disrupt microtubule-associated functions such as axonal transport (Staff et al., 2013). Microtubule stability is a complex process that can be affected by post translational modifications (PTMs) of α-tubulin. Tubulin PTMs, as well as microtubule dynamics and stability, play critical roles in neurons via the regulation of long-distance transport, microtubule severing, Ca2+ homeostasis and mitochondrial trafficking and energy production (Bär et al., 2022). In a previous study Pero et al. (2021) demonstrated that BTZ-induced peripheral neuropathy is contributed by pathogenic Δ2-tubulin accumulation, which affects both mitochondrial motility and axonal viability. However, whether the same mechanism mediates CFZ-dependent neurotoxicity remains to be understood. One hypothesis is that one of the main mechanistic differences resides indeed in a direct binding of BTZ to tubulin that CFZ did not show in an in silico structure screening assay (Malacrida et al., 2021).

Herein, we introduced a novel preclinical model of CFZ-induced peripheral neuropathy to compare its behavioural and morphological phenotype, as well as its proteome on ex vivo dorsal root ganglia (DRG), with a validated bortezomib-induced peripheral neuropathy (BIPN) model. Furthermore, to mechanistically explain the effect of either drug on both cytoskeleton as well as mitochondrial morphology and function, we used in vitro primary culture of DRG neurons to identify the initiating neurotoxic event, in order to select both the best therapeutic approach and window of opportunity for intervention.

2 | METHODS

2.1 | Animals and housing conditions

Animals underwent health evaluation shortly after arrival. Their care and husbandry were in compliance with national (D.L.vo n. 26/2014) and international laws and policies (EEC Council Directive 86/609, OJ L 358, 1, Dec 12, 1987; Guide for the Care and Use of Laboratory Animals, US National Research Council, 2011). Animals (8/10 old weeks, approximatively 20 g at the beginning of the study) were purchased from Envigo Laboratory (Udine, Italy) and were housed under controlled conditions (room temperature: 22°C ± 2°C, room relative humidity: 55% ± 10%, 24-h cycle of 12 h light/12 h dark, 7 AM to 7 PM). The mice had free access to food and water during the experiments. This study was approved by the Italian Ministry of Health (Approval Number 865/2023-PR).

In a preliminary study of chronic CFZ tolerability, a total of 10 female BALB/c mice (5 untreated controls and 5 CFZ-treated) were untreated or intravenously (i.v) treated with 2.0 mg kg^{-1} of CFZ twice a week on consecutive days for 4 weeks.

In the neurotoxicity study, after randomization based on the nerve conduction studies and behavioural tests, a total of 64 female BALB/c mice (21 untreated controls; 21 BTZ-treated; 22 CFZ-treated) were used for the neuropathy model comparison experiments. Of these, 25 (8 untreated controls; 8 BTZ-treated; and 9 CFZ-treated) were euthanised mid-treatment, whereas the other 39 (13 each group) were euthanised at the end of treatment. Animal studies are reported in compliance with the ARRIVE guidelines (Percie du Sert et al., 2020) and with the recommendations made by the British Journal of Pharmacology (Lilley et al., 2020). The operators were blinded to the treatment when performing behavioural tests and conduction studies.

CFZ (MedChemExpress, Monmouth Junction, NJ, USA) was administered at a dose of 2.0 mg kg^{-1} at a volume of 10 ml kg^{-1} (200 µl for a 20-g mouse) twice a week on two consecutive days (Cheung et al., 2021; Demo et al., 2007) for two (mid-treatment) or four (end-treatment) weeks, preceded by body weight measurements (i.v. CFZ: 2.0 mg/kg, i.v, diluted as a stock solution at 2 mg ml^{-1} in 5% DMSO, 5% tween 80, 40% PEG300, 50% saline solution, and then diluted 1:10 in Captisol 10% in a Citrate Buffer 25 mM pH 4 solution). BTZ (LC Laboratories, Woburn, MA, USA) was administered as previously described (Meregalli et al., 2015). The flowcharts for the studies containing information about drugs dosage and treatment regimen can be found in Figures S1 and S2.

2.2 | Non-invasive tests

Non-invasive tests were performed in both studies on all the animals at baseline (for randomization purposes), at mid-treatment (2 weeks) and at the end of treatment regimen (4 weeks). All behavioural tests were performed by a single blinded examiner.

2.3 | Nerve conduction studies

The development of BTZ- and CFZ-dependent neuropathy was assessed by evaluating the sensory conduction velocity (SCV) and sensory action potential amplitude (SAP) of the caudal and digital nerves, using an electromyography apparatus (Matrix Light, Micromed, Treviso, Italy), using subdermal needle electrodes. To measure SCV and sensory action potential (SAP), a pair of recording electrodes (cathode and anode) were placed at the base of the tail, whereas a pair of stimulating electrodes were placed 3.5 cm from the recording ones. Latencies were measured from stimulus onset, and peak-to-peak amplitudes were calculated. The nerve conduction velocity was calculated as the ratio of the distance between the recording and stimulating dipoles over the stimulus latency. All the neurophysiological determinations were performed with the animals under isoflurane anaesthesia along the whole procedure with continuous monitoring of vital signs and mice body temperature was kept constant via a thermostat heating pad (Ballarini et al., 2022; Monza et al., 2021).

2.4 | Dynamic aesthesiometer test

Behavioural tests to examine the neuropathic pain were performed after 2 and 4 weeks of BTZ and CFZ administrations by a blinded

examinator. Allodynia (mechanical sensitivity) was measured by Dynamic Aesthesiometer Test (Model 37450, Ugo Basile Biological Instruments, Comerio, Italy). Mice were placed in a clear plastic box with a wire mesh floor and allowed to habituate for 1 h and 30 min before testing. A pointed metallic filament of 0.5-mm diameter, which exerted a progressively increasing punctuate pressure, was applied to the mid plantar skin of each hind paw six times, reaching up to 15 g within 15 s. A cut-off time of 20 s was used. The pressure evoking a clear voluntary hind-paw withdrawal response was recorded automatically and taken as the mechanical nociceptive threshold (Li et al., 2023).

2.5 | Proteasome inhibition assay on peripheral blood mononuclear cells

Peripheral blood mononuclear cells (PBMCs) were isolated from blood samples by Lympholyte density separation. Cells were added to the lysis solution (50-mM HEPES, 5-mM EDTA, 150-mM NaCl and Triton-X 100 1% in water), vortexed, sonicated and subsequently centrifuged at 18.000×*g* for 15 min at 4°C. The samples were then processed for proteasome inhibition levels assessment right after lysis. Protein concentration was assessed by the Bradford assay with a Coomassie® Protein Assay Reagent Kit (Pierce, Thermo Scientific, Rockford, IL, USA). A fluorometric assay evaluated the proteasomal activity and the protein extract was incubated with N-succinyl-Leu-Leu-Val-Tyr-7-Amido-4- Methylcoumarin substrate (Sigma Aldrich, Milano, Italy) for 2 h. Proteasome activity was detected as a relative light unit generated from cleaved substrate in the reagent. Fluorescence (F) from each reaction was assessed with a microplate reader (excitation 380 nm and emission 460 nm) (BMG Labtech, Otrenberg, Germany). The proteasome activity (PA) was calculated as % PA = 100 × (F BTZ − F Substrate)/(F Control − F Substrate) and proteasome inhibition was expressed as 100-PA.

2.6 | Sampling and processing of organs

After 2 and 4 weeks of treatment, animals were euthanized by inducing and maintaining deep anaesthesia with isoflurane until the loss of the reflex was confirmed. Terminal blood collection was then performed via the inferior vena cava, followed by exsanguination. Death was confirmed by the total absence of respiration and cardiac activity prior to tissue harvesting, ensuring permanent cessation of circulation. At each time point, sciatic nerves, caudal nerves and skin biopsies were collected from three animals per groups and fixed with 4% paraformaldehyde and 2% glutaraldehyde in a phosphate buffer solution (0.12 M), post-fixed in OsO_4 and epoxy resin embedded to be ready for morphological and morphometric examination. Samples were stored at room temperature until cut.

2.7 | Morphological and morphometric evaluation

Sciatic and caudal nerves, once collected and processed for optical and electron microscopy according to previously reported protocols for morphological analysis (Ballarini et al., 2022; Cavaletti et al., 1992), were then cut in 1.5-μm-thick semi-thin sections of the resin embedded nerves (three animals per group), stained with methylene blue and examined with a Nexscope Ne920 AUTO light microscope using a 40X magnification objective for morphological assessment and a 60X magnification objective for morphometric evaluation (TiEsseLab Srl, Milano, Italy). The images acquired were then analysed using a computer-assisted image analyser using the Image Pro-Plus software (Media Cybernetics, Rockville, MD, USA). The density (fibres mm^{-2}), the external and the axonal diameters of myelinated fibres (used to calculate the histogram of fibre distribution) were measured in randomly selected sections according to previously reported methods (Ballarini et al., 2022; Cavaletti et al., 1992).

Seventy-nanometer ultrathin sections of the sciatic nerves were cut with an ultramicrotome (Ultracut E, Reichert-Jung) and used for morphological observation at the electron microscope (Philips CM 10 e Itachi HT7800).

2.8 | Intraepidermal nerve fibre density assessment

At middle and at end treatment glabrous skin punch biopsies from the plantar hind paw were collected to evaluate the intraepidermal nerve fibre (IENF) density. The samples were fixed in PLP 2%, cryoprotected and kept at −20°C until cutting. 20-um-thick slices were serially sectioned, and three sections/animals were immunostained with rabbit polyclonal anti-protein gene product 9.5 (PGP 9.5) (Proteintech, Rosemont, IL, USA) using a free-floating protocol as previously described (Meregalli et al., 2018). The total number of intraepidermal nerve fibres (IENFs) positive to PGP 9.5 crossing the dermal-epidermal junction was counted using a light microscope at 40X magnification (Nexcope Ne920 AUTO light microscope, TiEsseLab Srl, Milano, Italy) by the same blinded examiner. Intraepidermal nerve fibre density was expressed as the ratio between the number of positive intraepidermal nerve fibres (IENFs) and the length of epidermis (mm) (Canta et al., 2020).

2.9 | Protein digestion for mass spectrometry

Extracted proteins from mouse DRG tissue were quantified using the Bradford assay and enzymatically digested for subsequent LC-MS/MS analysis. Digestion was performed using S-trap TM Micro and Mini spin columns (ProtiFi, Fairport, NY, USA), selected based on the total initial protein amount. These columns were used to concentrate samples and remove detergent interference, following the manufacturer's protocol with minor modifications (Ludwig et al., 2018). In particular,

Tris phosphate was used in place of TEAB buffer (Triethylammonium bicarbonate) both in the SDS lysis buffer 2X (10% SDS, 100-mM Tris-phosphate, pH 8.5) and in the binding buffer (90% aqueous methanol with a final concentration of 100 mM Tris phosphate, pH 7.55), whereas ammonium bicarbonate 50 mM was used as digestion buffer. Following sample lysis with the SDS lysis buffer, disulphide bonds were reduced with DL-Dithiothreitol (DTT) (Sigma-Aldrich, St. Louis, MO, USA, ≥99.5%) at the final concentration of 20 mM and incubated for 45 min at 56°C. Then, iodoacetamide (IAA) (Sigma-Aldrich, St. Louis, MO, USA) was added to a final concentration of 40 mM, and samples were incubated at room temperature for 30 min to facilitate carbamidomethylation. The reaction mixture was then acidified with aqueous phosphoric acid (final concentration: 1.2%) and combined with a binding buffer at a 1:6 (v/v) ratio. The sample was loaded into the spin column for protein trapping and subjected to overnight digestion with trypsin (porcine pancreas, Sigma-Aldrich, St. Louis, MO, USA) at 37°C.

The following day, peptides were sequentially eluted using 50 mM ammonium bicarbonate, 0.2% formic acid (FA) and finally, 50% aqueous acetonitrile for hydrophobic peptide recovery. Pooled eluates from each sample were dried using a vacuum centrifugal evaporator (Hetovac, Savant, Thermo Fisher Scientific, Waltham, MA, USA) and resuspended in 50 µl of 0.1% formic acid. Peptide content was quantified using a NanoDrop spectrophotometer (NanoDrop OneC, Thermo Fisher Scientific, Wilmington, DE, USA).

2.10 | Mass spectrometry analysis

For each sample, 400 ng of tryptic peptides was injected in triplicate into Evosep One (Evosep Biosystems, Odense, Denmark) LC system coupled online with timsTOF fleXTM (Bruker Daltonics, Bremen, Germany) mass spectrometer, as already reported (with some modifications) (Previtali et al., 2023). Peptides were loaded into a disposable trap column, Evotip PureTM (Evosep Biosystems, Odense, Denmark) following the manufacturer protocol. Desalted and concentrated peptides were separated into an analytical 8-cm column (PepSep C18, Bruker Daltonics, Bremen, Germany, 8-cm performance column, particle size of 1.5 µm and internal diameter of 150 µm) at a temperature of 40°C. A gradient of 21 min (60 SPD) with solvent A (0.1% FA) and solvent B (ACN + 0.1% FA) was used for the separation. The eluted peptides were ionized using a nanoCaptiveSpray™ (Bruker Daltonics). The mass spectrometer was operated in DIA (Data Independent Acquisition)-PASEF (Parallel Accumulation-Serial Fragmentation) mode. Ions were scanned in positive mode, over an m/z of 100–1700 and a mobility range of 0.80–1.30 $V{\cdot}s\ cm^{-2}$. Dry gas flow was 3.0 $l\ min^{-1}$ at 180°C and capillary voltage was 1600 V. For tandem mass PASEF analysis, the cluster of mono-charged ions was excluded to reduce the complexity of MS2 spectra using the following parameters: mass range 348.1–973.1 Da and 0.80–1.22 1/K0, the estimated cycle time for each PASEF analysis was 1.17 s with a total of 10 cycles using DIA windows of 25 Da.

The mass spectrometer was calibrated for mass accuracy using a mix of 10 standards with known mass (MMI-L Low Concentration Tuning Mix, Agilent Technologies, Santa Clara, CA, USA). With nano-source, mass and ion mobility calibration was performed using three specific lock masses (622.0290, 922.0098 and 1221.9906 m/z) applied on a filter.

2.11 | Proteomic data processing

Raw data were elaborated by using SpectronautTM (v.19.7, https://biognosys.com) following a library-free processing method. A mouse database with protein isoforms (Swissprot, downloaded on 12 February 2025) was used. The parameters were set as follows: trypsin as the enzyme, carbamidomethyl (C) as the fixed modifications, acetylation (protein N-term) and oxidation (M) as the variable modifications, 1% FDR at precursor and protein levels. Abundance values were automatically normalized across runs. Proteins were considered identified only if they had at least one significant unique peptide.

2.12 | Proteomic data statistical analysis and functional annotation

Processed proteomic data were analysed using Metaboanalyst open-source platform (www.metaboanalyst.ca). Features with more than 20% of missing values were excluded, and missing values were replaced with limit of detection (LoD). Some proteins (keratins, myosins) that are abundantly expressed in the skin and in both smooth and striated muscles—signs of possible contamination and of no interest in our study—were excluded from further analysis. Data were then normalized and transformed into logarithmic values (Base 10). Statistical tests (one-way ANOVA and *t* tests) were performed in Metaboanalyst using False Discovery Rate (FDR) correction and a 0.01 threshold for significance. Each condition (BTZ and CFZ) was compared with control and between each other and a 1.5-fold cut-off in protein expression changes, as well as a significance threshold of 0.01 (FDR), were used for volcano plots and feature extraction.

Each list of differentially expressed proteins was compared with the others using Venny 2.1.0 (https://bioinfogp.cnb.csic.es/tools/venny/index.html) to find similarities. Functional annotation was then performed on these lists to evaluate the significantly enriched biological processes ($p < 0.05$ FDR) using the Gene Ontology Resource (2025-03-16: 40.214) (Gene Ontology). Protein association networks were built using STRING database (12.0) (STRING).

2.13 | Sensory neuron primary cultures

Cultures were obtained from dorsal root ganglia (DRG) of 12–16 weeks old C57BL/6 male mice (approximatively 30 g at the beginning of the study) were purchased from Envigo Laboratory (Udine, Italy). All experimental procedures were carried out in compliance with the Animal Research: Reporting of In Vivo Experiments (ARRIVE 2.0) guidelines and in accordance with National Institute of Health guidelines for animal care and use of Laboratory animals (DL 2016, Italian Ministry of Health approval protocol FB7CC.N.QGE). Briefly,

after dissection, DRGs were digested with 1.25 mg ml^{-1} of collagenase and 10 mg ml^{-1} of DNase for 75 min at 37°C. DRGs were mechanically triturated, and then, primary neurons were isolated with a 30% bovine serum albumin (BSA) gradient and plated on laminin coated dishes. Neurons were cultured in DMEM-F12 medium supplemented with B27, penicillin–streptomycin and L-Glutamine and maintained for 48 h. Neuron cultures were then treated with either drug for up to 48 h before proceeding with subsequent analyses. For Seahorse assay and mitochondrial trafficking experiments, DRG from 8- to 10-week-old C57Bl/6J mice were dissected, dissociated and plated in a live imaging dishes plate or in XF24-well microplates as previously described (Pero et al., 2021; Shin et al., 2021).

2.14 | Drugs and treatment

BTZ and CFZ, coming from the same batches used for the in vivo experiments, were dissolved in dimethyl sulfoxide (DMSO) to make a stock solution of 2.6 and 5 mM, respectively. These stock solutions were appropriately diluted with cell culture medium to obtain the working concentrations of 10 nM for BTZ and 60 nM for CFZ.

2.15 | MTT assay

RPMI-8226 multiple myeloma cells were cultured in DMEM supplemented with 10% fetal bovine serum, 1% L-glutamine, 1% Penicillin and Streptomycin (Euroclone, Pero, Italy). Cells were incubated at 37°C and 5% CO_2 in a humidified incubator for maintenance, then seeded in 96-well plates at 10^4 cells per well density to perform the assay. Cells were then treated with increasing concentrations of BTZ or CFZ (1–100 nM). After 24 h of treatment, a 5 mg ml^{-1} solution of 3-(4,5-dimethylthiazol-2-yl)-2,5-diphenyltetrazolium bromide (MTT) (Sigma-Aldrich, St. Louis, MO, USA) was added directly to culture medium at a final concentration of 0.5 mg ml^{-1}. Plates were incubated at 37°C for 4 h and centrifuged at 600*g*. Culture medium was removed, and formazan crystals were solubilized in acidified 2-propanol (0.3% HCl). Absorbance of the solution was measured at 560 nm in a multiplate reader (BMG-Labtech, Ortenberg, Germany).

2.16 | Live cytotoxicity assay with nanolive system

RPMI-8226 multiple myeloma cells were cultured and maintained in complete media as previously described. After coating with Poly-L-lysine (Sigma, P2636; Sigma-Aldrich, St. Louis, MO, United States), cells were seeded at a density of 3*10^4 cells per dish on µ-Dish 35 mm (Nanolive imaging, 80136; Nanolive SA, Tolochenaz, Switzerland). After 24 h, cells were either left untreated or treated with BTZ 10 nM or CFZ 60 nM, for 24 h, whereas an image was recorded every 30 min by Nanolive CX-60 Fucus (Nanolive Imaging System). The analysis of living, apoptotic and necrotic cells were performed by Live Cytotoxicity Assay by Eve software (Nanolive System).

2.17 | Proteasome inhibition assay on dorsal root ganglion (DRG) neuronal cultures

DRG neuron cultures were either left untreated or treated with BTZ 10 nM and CFZ 60 nM for 24 h. Afterwards, neuronal cultures were washed with cold phosphate buffered saline (PBS) and then 50 µl of lysis buffer (5-mM Hepes pH 7.5, 150-mM NaCl, 10% Glycerol, 1% Triton X-100, 1.5-mM MgCl2 and 5-mM EGTA) was added to each dish. After mechanical scraping the suspension was collected and the neuron lysates were clarified with a centrifuge at the equivalent value 13,500 g for 15 min at 4°C. Protein content was quantified using the Bradford assay (Sigma-Aldrich). Forty micrograms of proteins was then loaded in black 96-well plates with 10 µl of 10X proteasome buffer (250 mM Hepes pH 7.5, 5 mM EDTA pH 8.0, 0.5% NP-40, 0.01% SDS) and 10 µl of proteasome substrate (7.6 mg/ml N-SuccinylLeu-Leu-Val-Tyr-7-Amido-4-Methylcoumarin) (Sigma-Aldrich). After 2 h at 37°C, fluorescence was quantified in a microplate reader (Ex: 380 nm; Em: 460 nm) (BMG-Labtech, Germany).

2.18 | Survival and neurite elongation assays

Neuron survival was evaluated by taking pictures of the same field, through a camera linked to an inverted microscope at baseline before and 24 h after treatment with BTZ 10 nM and CFZ 60 nM (control cells were left untreated). Viable neurons, characterized by a birefringent outline, which is absent in dead cells, were manually counted using ImageJ software. The cell death induced by BTZ or CFZ treatment was calculated and compared to the ones obtained in the untreated control culture at different time points. Neurite elongation was measured in the same pictures used for neuron viability. At least 30 neurites for each picture were measured using the NeuronJ plugin for ImageJ. Each experiment was performed three times to validate the results.

2.19 | Calcium measurements

Cultured DRG neurons were either untreated or treated with BTZ 10 nM and CFZ 60 nM for 24 h before performing the calcium measurements. Fura-2, AM form, was purchased from ThermoFisher (Cat. F1201). For mitochondrial calcium dynamics assessment, mt-fura-2.3, a modified version of mt-fura-2, was used (de Nadai et al., 2021; Pendin et al., 2019). The total amount of neurons derived from one mouse's DRGs were plated onto 10 round coverslips (diameter 24 mm) and loaded with 5 µM Fura-2/AM (Cat. No. F1201, Life Technologies, Milan, Italy) in the presence of 0.005% Pluronic F-127 (Cat. No. P6867, Life Technologies, Milan, Italy) and 10 µM sulfinpyrazone (Cat. S9509, Sigma) in Ca2+-containing Tyrode solution (TS). TS composition was (in mM): 154 NaCl, 4 KCl, 2 CaCl2, 1 MgCl2, 5 HEPES, 5.5 glucose and NaOH to pH 7.4. All calcium experiments were performed on three different cultures.

Imaging was performed using an epifluorescent Leica DMI6000B microscope equipped with an S Fluor 40X/1.3 objective, a Polychrome V monochromator (Till Photonics, Munich, Germany). For imaging of mitochondria, an internal lens with a 1.6 optical increment was used. Images were acquired by a Hamamatsu cooled CCD camera (Hamamatsu Photonics, Hamamatsu City, Japan) and registered using MetaFluor software (Molecular Devices, Sunnyvale, CA, USA). Image time series were analysed with ImageJ (Rasband W.S., NIH, Bethesda MD, USA) and OriginPro 9.1 software (OriginLab, MA, USA) to obtain the background subtracted ratio of the mean pixel intensity within a region of interest encompassing a neuronal cell body. Finally, data in traces expressed as 340/380 nm ratio were normalized according to the formula $RN = \Delta F/F0$. The experimental curves obtained in different conditions were compared using a modified Chi-squared method that allows to calculate the overall p value and the p values for individual pairs of points (Hristova & Wimley, 2023).

2.20 | Primary and secondary antibodies used for Western blot

Primary antibodies used for western blot experiments were the following: anti-Δ2 (rabbit) (Sigma-Aldrich, Cat.# AB3203, RRID:AB_177351), anti-acetylated tubulin (mouse) (Sigma-Aldrich, St. Louis, MO, USA, Cat.# T-6793, RRID:AB_477585), anti-MAP 2 (mouse) (Merck-Millipore, Darmstadt, Germany, Cat.# MAB1567), anti-VDAC (rabbit) (Abcam, Cambridge, UK, Cat.# ab15895, RRID:AB_2214787) and anti-actin (mouse; rabbit) (Merck-Millipore, Darmstadt, Germany, Cat.# A1978, RRID:AB_476692; Sigma-Aldrich, St. Louis, MO, USA, Cat.# A5060, RRID:AB_476738). Secondary antibodies used for western blot experiments were anti-mouse-HRP (Merck-Millipore, Darmstadt, Germany, cat. # AP181P, RRID:AB_11214094) and anti-rabbit-HRP (Perkin Elmer, Waltham, MA, USA, Cat. # NEF812001EA, RRID:AB_2571640). The Immuno-related procedures used comply with the recommendations made by the British Journal of Pharmacology (Alexander et al., 2018).

2.21 | Western blotting

Total protein extracts were obtained from DRG neuron cultures treated for 10 or 24 h with either drug using radio immunoprecipitation assay (RIPA) lysis buffer. Proteins were then separated in a graded 4–20% acrylamide SDS-PAGE and after electrophoresis, proteins were transferred to a nitrocellulose membrane. Briefly, the membrane was blocked with either 5% non-fat milk or 5% BSA blocking solution, and then, the membrane was exposed to the respective primary antibodies. After incubation, the membrane was incubated with respective horseradish peroxidase-conjugated secondary antibodies. At last, immunoreactive proteins were visualized using an ECL chemiluminescence system (Amersham, Sullivan County, TE, USA).

2.22 | Immunofluorescence

Cultured DRG neurons were either untreated or treated with CFZ or BTZ for 10 or 24 h before fixation with 4% paraformaldehyde—diluted in 0.12 M phosphate buffer (with 30% glycerol) and heated at 37°C—for 10 min at room temperature. Cells were then washed with PBS heated at 37°C and then incubated 1 h at 37°C with the following primary antibodies: Δ2-tubulin IgG rabbit (Merck-Millipore, Cat.# AB3203, RRID:AB_177351) 1:200 and β3-tubulin, IgG mouse (clone Tuj1, Biolegend, San Diego, CA, USA, Cat.# 801201, RRID:AB_2313773) 1:1000. The secondary antibodies used were goat anti-mouse IgG Alexa488 and goat anti-rabbit IgG Alexa555. Images were captured with a LSM 980 laser scanning confocal microscope (Zeiss, Oberkochen, Germany) with a 40×/1.3 NA oil immersion objective using a 488 nm and 561 nm solid-state laser line. Laser power and photomultiplier gain were adjusted to minimize background noise rate and saturated pixels and kept constant for all the acquisitions.

2.23 | Image processing and degeneration index calculations

Images were processed and analysed with Fiji software. By using the appropriate modules, images have been thresholded, the region of interest has been defined and the mean fluorescence intensity of the two channels analysed. To quantify axonal degeneration, images were binarized and the total area occupied by the axons (total axonal area) or the area occupied by fragmented axons or axons with massive varicosities (degenerating axonal area) have been evaluated. Degeneration index has been calculated only on the β3-tubulin channel and corresponds to the ratio between degenerating and total axonal area.

2.24 | In silico analysis of mitochondrial network morphology

To investigate the morphology of the mitochondrial network in DRGs cultures, we applied the Mitochondrial Network analysis (MiNA), an ImageJ based utility to aid in quantitatively describing the appearance of different parameters related to mitochondrial morphology, as we previously described (Calabrese et al., 2020; Contino et al., 2020; Panuzzo et al., 2023). Cells were immunostained with DAPI (for nuclei detection), MAP 2 and TOM20 to respectively identify neuronal cells and their mitochondria and images were collected by Zeiss LSM 710 confocal microscope and analysed by MiNA. Briefly, images were opened on ImageJ and processed as follows: 1-Process/Filters/UnsharpMask; 2-Process/EnhanceLocal Contrast (CLAHE); 3-Process/Filters/Median; 4-Process/Binary/MakeBinary; 5-Process/Binary/Skeletonize; 6-Analyze/Skeleton/AnalyzeSkeleton(2D/3D); 7-Plugins/StuartLab/MiNAScripts/MiNAAnalyzeMorphology (for the entire workflow refer to Valente et al., 2017).

2.25 | Seahorse bioenergetic analysis

Mitochondrial respiration in cells was measured using a Seahorse Bioscience XF24 extracellular flux analyser, Agilent, Santa Clara, CA, USA as previously described (Morcillo et al., 2024). DRG cells were seeded in XF24-well microplates. Before initiation of measurements, cells were rinsed and incubated with XF base medium (Agilent 102353-100) supplemented with 25-mM glucose and 2-mM sodium pyruvate (Thermo Fisher Scientific, Waltham, MA, USA, 11360070), pH 7.4. After 45 min incubation in a CO_2-free incubator at 37°C, the oxygen consumption rate (OCR) was measured at the basal state and after sequential injection of 1 μM oligomycin (ATP synthase inhibitor; Sigma-Aldrich, St. Louis, MO, USA, 75351), 0.75-μM carbonyl cyanide-p trifluoromethoxyphenylhydrazone (FCCP; uncoupler; Sigma-Aldrich, St. Louis, MO, USA, C2920), and 1-mM rotenone/antimycin A (complex I/III inhibitor; Sigma-Aldrich, St. Louis, MO, USA, R8875 and A8674, respectively). All OCR values were normalized to cell number after the experiment. The readouts were used to define the bioenergetic parameters as follows: ATP-linked OCR = OCR Baseline-OCR Oligomycin. Measurements were performed on at least three technical replicates, and the experiment was repeated at least three times (biological replicates). The Wave report generator (Agilent) was used for analysis.

2.26 | Mitochondrial membrane potential measurements

Cells were incubated for 30 min at 37°C in culture condition with 50-nM MitoTracker TM Red CMXRos (Thermo Fisher Scientific) and 25-nM MitoTracker TM Green FM (Thermo Fisher Scientific) and subsequently washed twice in PBS and mounted on glass slides with a 90% (v/v) glycerol/PBS solution. Images acquisition and analysis Images were acquired using Zeiss LSM 710 confocal laser-scanning microscope (Zeiss) using a 25×, 0.9 N/A oil-immersion objective. Laser intensities and acquisition parameters were held constant throughout each experiment. Confocal microscopy fields were analysed using specific homemade designed macro with ImageJ (https://imagej.nih.gov/ij/) software. Briefly, mitochondrial size quantification was performed measuring the integrated density (ID) of green signal normalized over the analysed area and mitochondrial activity was performed measuring the integrated density (ID) of red signal over green signal ratio. All the data obtained derived from at least 10 fields per sample. Statistical analysis and graphs were analysed using GraphPad Prism (GraphPad Software, Inc.).

2.27 | Mitochondria motility assays

Dissociated adult DRG neurons were transduced at 24 h after plating with Mito-DsRed lentiviruses to track mitochondria motility. At 5 days in vitro (DIV) neurons were live-imaged using an epifluorescence microscope (Nikon Ti), equipped with a temperature-controlled (37°C) CO_2 incubator. Proximal regions from intact axons (within 200 μm from the cell body) were selected for imaging, and movies were acquired at 2 s per frame for 10 min to track mitochondria. Kymographs were generated manually with a Fiji's plugin by tracing the proximal axon using a segmented line tool. Mitochondria dynamic states were identified on kymographs and classified as follows: mitochondria were defined as stationary (ST) if fixed in an immobile state for the entire length of the movie. Dynamic mitochondria were subclassified as dynamic pausing, if showing persistent and short oscillatory movements in either direction (approximately <3 μm), or anterograde (AR) and retrograde (RR) running if moving for short or longer distances in either direction (approximately >3 μm). The number of different movement states per movie was scored and quantified on kymographs. The density of each dynamic state was reported as a percentage of total density to normalize for fluctuations in total numbers (Pero et al., 2021) and then normalized to control values.

2.28 | Statistical analysis

Data and statistical analysis complied with the recommendations of the *British Journal of Pharmacology* on experimental design and analysis in pharmacology (Curtis et al., 2025).

All assessments were made by researchers blinded to animal treatments. Sample size for in vivo experiments was calculated on the basis of our laboratory neurophysiological reference values, our primary end point to evaluate onset of peripheral neuropathy (Monza et al., 2021). We considered a two-sided 5% alpha and a 80% power as set, therefore the sample size is seven animals per group. In each individual experiment, the sample size was increased above this number considering eventual fatalities due to chemotherapy administration for each death time (mid treatment and end treatment). Moreover, additional animals were included in each group, in order to perform histopathological and multiple molecular analyses on enough animals to produce scientifically robust data as previously published (Pozzi et al., 2020).

In vitro experiments were conducted using primary cultures of adult mouse Dorsal Root Ganglion (DRG) neurons. Obtaining enough viable neurons for necessitated the killing of multiple animals. To adhere strictly to ethical guidelines and legislative requirements while maintaining sufficient statistical rigour, we adopted a smaller sample size ($n < 5$) in peculiar experiments, as already published (Pero et al., 2021). This decision was primarily driven by the Principle of Reduction (one of the internationally recognized 3Rs: Replacement, Reduction, Refinement). The 3Rs are a mandatory ethical and legal requirement in animal experimentation, codified in the European Union Directive 2010/63/EU and its subsequent national transpositions (the Italian legislative decree D.Lgs. 26/2014). Given the resource-intensive nature of these assays, increasing the number of independent biological replicates for every parameter was deemed unsustainable in terms of analytical costs and time. To preserve the overall experimental framework, these data were treated as hypothesis-generating insights. Consequently, we focused on descriptive trends rather than formal comparative analysis.

Results were expressed as mean ± (SEM), median ± interquartile range with whiskers at minimum/maximum or as value distributions. The *n* number of independent values used for statistical analysis was stated within each figure legend. Statistical tests used depended on the results and are listed within the legends below each figure. Briefly, either parametric (ANOVA) or non-parametric (U Mann–Whitney, Kruskal–Wallis) tests were used based on the analysed data, together with the appropriate post hoc comparisons. Post-hoc tests were run only if F achieved P<0.05 and there was no significant variance inhomogeneity. Calcium fluctuation traces were analysed using a modified Chi-squared method that allows to calculate the overall *p* value and the *p* values for individual pairs of points. Proteomic data statistical analyses are detailed in the specific section. GraphPad Prism 8 statistical package (GraphPad Software, San Diego, CA, United States) was generally used to compute *p* values, and $p < 0.05$ was considered significant.

2.29 | Nomenclature of targets and Ligands

Key protein targets and ligands in this article are hyperlinked to corresponding entries in the IUPHAR/BPS Guide to PHARMACOLOGY http://www.guidetopharmacology.org and are permanently archived in the Concise Guide to PHARMACOLOGY 2025/26 (Alexander et al., 2025).

3 | RESULTS

3.1 | Identification of the Carfilzomib (CFZ) dose to be used for the neurotoxicity study

Because literature data do not present chronic treatment schedules for the study of CFZ neurotoxicity, a preliminary study was conducted testing the known anti-tumour dose for a chronic period. Treatment dosage and regimen for CFZ were evaluated in vivo in female BALB/C mice (Figure S1a). Briefly, the final dose of 2.0 mg kg^{-1} was chosen based on the capability of inducing at least 80% inhibition of the proteasome complex in peripheral blood mononuclear cells (PBMC) 1 h after the last injection of CFZ. These cells were used for proteasome levels analysis because they allow for the systemic evaluation of proteasome inhibitors efficacy and are collected through minimally invasive peripheral blood sampling and partially mimic the inhibition levels in the neural tissues in preclinical models (PMID: 24335344). This 80% inhibition parameter, which arose from clinical evidence of patients treated with BTZ, has been the criterion of choice to define the efficacy of the preclinical model of bortezomib-induced peripheral neuropathy (BIPN) used in this work as well as in the literature (Figure S1b) (Adams & Kauffman, 2004; Alsina et al., 2012; O'Connor et al., 2009; Siegel et al., 2012). Good tolerability was also tested by measuring the mouse body weight at regular intervals (Figure S1c).

3.2 | Treatment with carfilzomib (CFZ) results in a less severe peripheral neurotoxicity phenotype than bortezomib (BTZ)

Following the identification of the dose of CFZ for the neurotoxicity study, we compared the two models of neuropathy induced by CFZ and BTZ.

Animals were injected with either BTZ or CFZ twice per week for 4 weeks, with CFZ injections delivered in consecutive days, an approach that mimics the clinic (Figure S2a) (Siegel et al., 2012). CFZ administration resulted in an initial reaction to the first round of injections, with a loss of weight registered within the first week of measurements; after this rapid reaction, the weight stabilized over time to control levels. BTZ administration, albeit well tolerated by the animals with no deaths reported, resulted in chronic toxicity developed over time as highlighted by a significant decrease in weight compared to both controls and mice treated with CFZ at the end of treatment (Figure S2b). During the physical examination, occasional piloerection was observed in some mice the day following BTZ administration. Animals' behaviour was otherwise normal, and no other remarkable evidence of general toxicity was observed.

Neurophysiological evaluations (i.e., targeting large fibre involvement) and mechanical threshold measurements (i.e., targeting small fibre involvement) were performed at mid-treatment and at the end of treatment to pinpoint the onset of peripheral neurotoxicity and the related neuropathic pain, respectively. At mid-treatment, no significant neurophysiological or behavioural differences were observed among the compared groups (Figure 1a,c[i]). However, at the end of treatment, the cohort treated with BTZ exhibited a significant decrease in sensory action potential amplitude and sensory conduction velocity in the caudal nerve compared to control animals, indicating deterioration of larger nerve fibres. On the other hand, CFZ treated animals showed no significant change in either sensory action amplitude or sensory conduction velocity compared to controls (Figure 1b).

Moreover, treatment with BTZ induced a strong mechanical allodynia indicated by a significant decrease in mechanical thresholds measured with dynamic plantar test compared to control animals, whereas CFZ-treated ones exhibited milder, albeit significant, allodynia at the end of treatment (Figure 1c[ii]).

Finally, no significant neurophysiological alterations were observed in digital nerves at any point of the treatment with either drug (Figure S3).

3.3 | Bortezomib (BTZ) causes significant nerve fibre degeneration compared to treatment with carfilzomib (CFZ)

Histopathological studies were performed on myelinated fibres of caudal and sciatic nerves using both morphological and

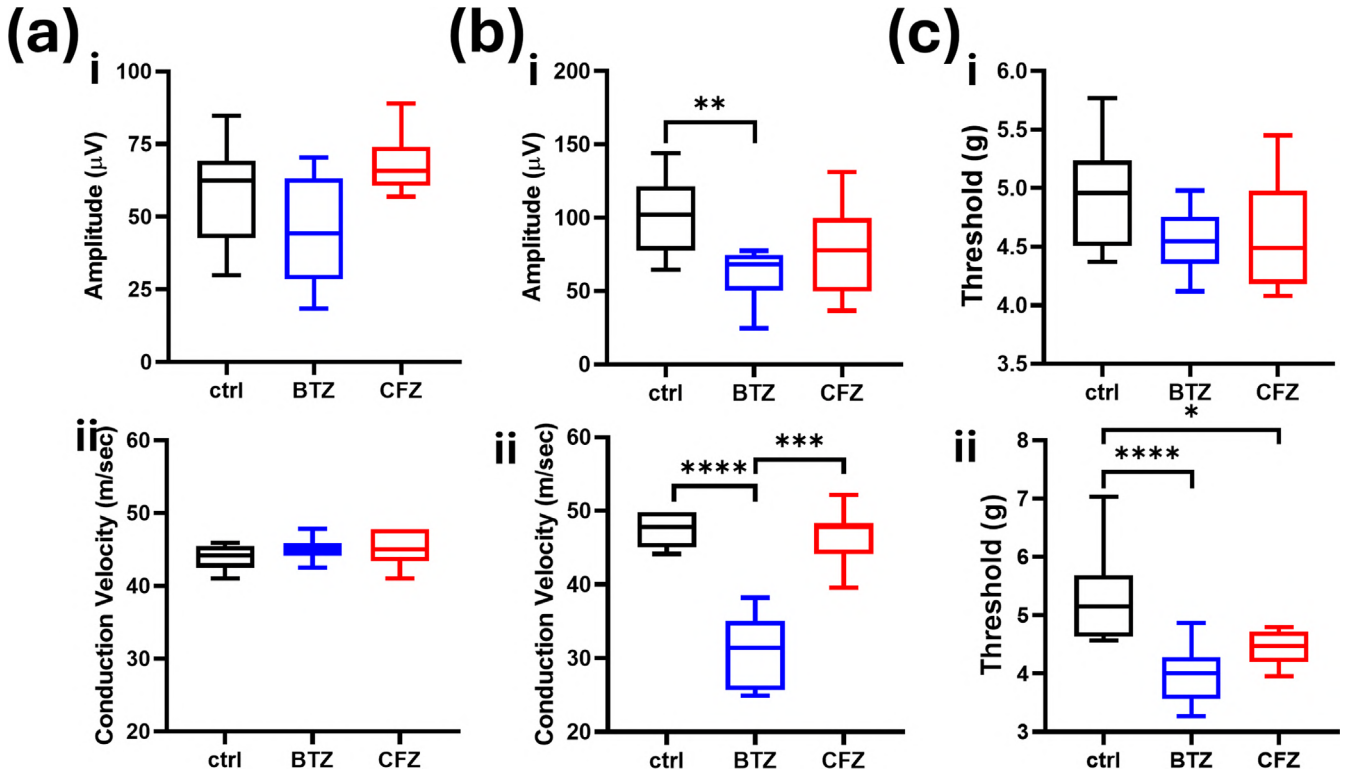

FIGURE 1 Behavioural tests to assess peripheral neuropathy development. (a) Box and whiskers plots showing sensory action potential amplitude (i) and sensory conduction velocity (ii) of the caudal nerve at mid-treatment. (b) Box and whiskers plots showing sensory action potential amplitude (i) and sensory conduction velocity (ii) of the caudal nerve at the end of treatment. (c) Box and whiskers plots showing the mechanical threshold of animals tested with the dynamic plantar test at mid-treatment (i) and at the end (ii) of treatment. $n = 8$ (BTZ, ctrl), 6 (CFZ) in plots in Ai, Aii, Ci. $n = 13$ (ctrl), 12 (BTZ), 10 (CFZ) in plots in Bi, Bii, Cii. Data in all plots are represented as box and whiskers, where the box indicates the median value and the interquartile range, whereas the whiskers indicate the minimum and maximum values. All groups were compared using Kruskal–Wallis with Dunn's multiple comparison post hoc test. *$p < 0.05$; **$p < 0.01$; ***$p < 0.001$; ****$p < 0.0001$. BTZ, bortezomib; CFZ, carfilzomib, ctrl, control

morphometrical analyses. In addition, to assess any change in the amount of non-myelinated nociceptive fibres, the density of the fibres innervating the hind paw skin was evaluated at middle and at the end of treatment.

Chronic administration of BTZ induced visible alterations already at mid-treatment: Light microscope morphological analysis of both caudal and sciatic nerves showed nerve fibre degeneration, with complete collapse of some fibres in both examined nerves (Figure 2a,e). These morphological alterations resulted in a decrease in the density of fibres – predominantly larger ones—within both caudal (Figure 2b,c) and sciatic nerves (Figure 2f,g). Moreover, the density of small unmyelinated fibres innervating the skin also decreased (Figure 2d). Conversely, the cohort treated with CFZ showed no signs of damage at this stage, with all parameters comparable to untreated control animals.

At the end of the treatment period, the axonopathy induced by BTZ steeply increased in severity. The collapse of nerve fibres was even more evident in both nerves (Figure 3a,e) with further decrease in the density of myelinated fibres of all sizes within the caudal (Figure 3b,c) and sciatic (Figure 3f,g) nerves as well as the unmyelinated ones innervating the skin (Figure 3d). At this time-point, CFZ treatment began to show the first morphological signs of neuropathy in the caudal nerve: a moderate decrease in the density of myelinated fibres was observed compared to control animals. Its severity, however, was evidently milder than the one observed in the BTZ treated cohort (Figure 3a,c) and we could not observe any decrease in the number of unmyelinated fibres versus control animals (Figure 3d). The situation in the sciatic nerve was similar to that of the caudal one: again, CFZ treatment showed signs of degeneration versus control that nevertheless were significantly milder than those caused by BTZ (Figure 3e,g). Investigation of fibre ultrastructure by transmission electron microscopy (TEM) confirmed the presence of degenerated fibres in samples treated with both drugs (Figure 3h).

3.4 | Bortezomib (BTZ) but not carfilzomib (CFZ) downregulates proteins involved in maintaining axon integrity and axonal transport

To dissect potential molecular changes occurring after treatment with proteasome inhibitors, we performed an untargeted proteomic analysis on DRG tissue samples collected from six mice per condition at the

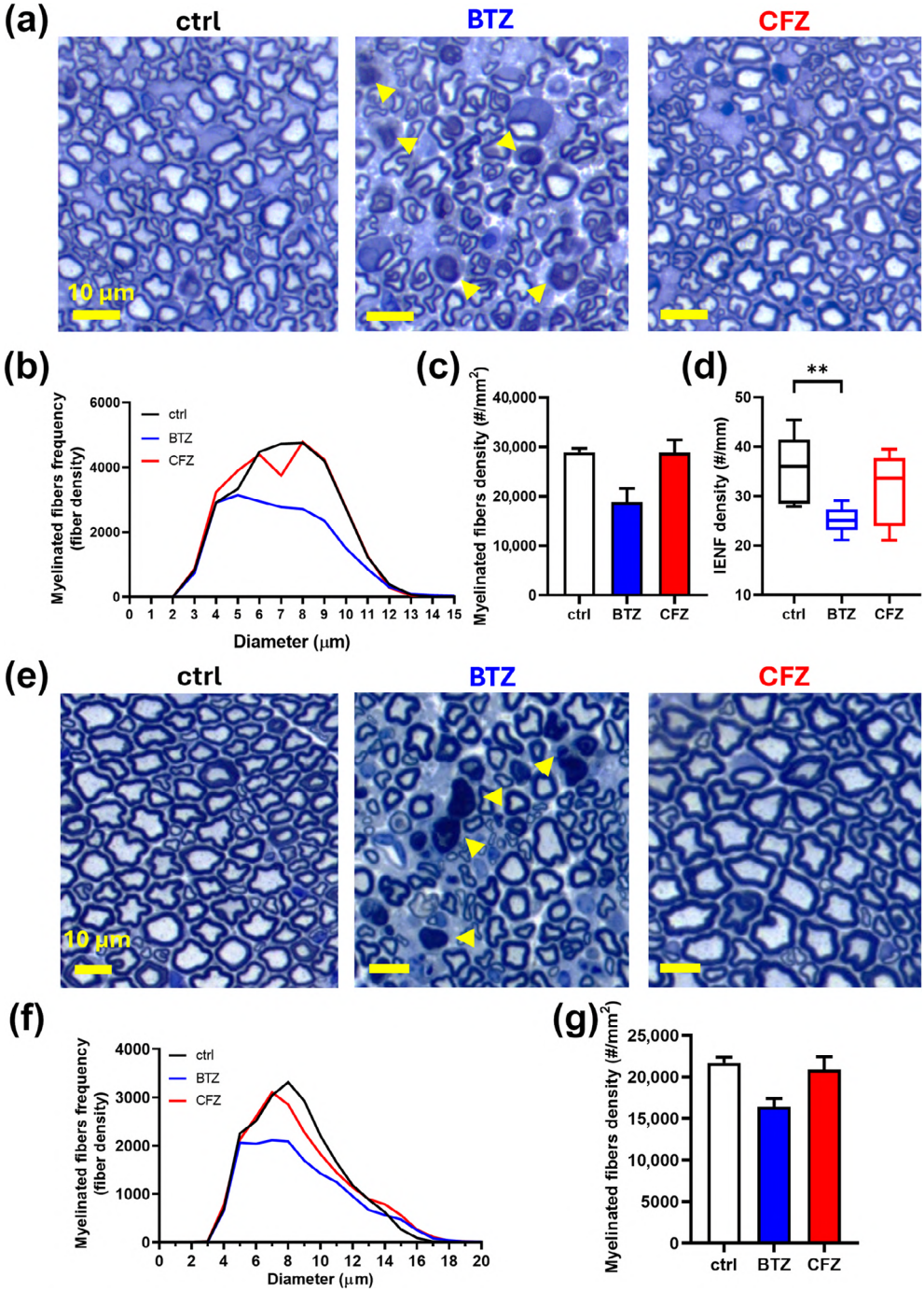

FIGURE 2 Bortezomib (BTZ) but not carfilzomib (CFZ) already causes loss of nerve fibres at mid-treatment. (a) Representative images of caudal nerves of untreated control animals and animals treated with BTZ and CFZ. Arrows indicate degenerated fibres. Scale bar: 10 µm. (b) Plot showing the distribution of the diameter of myelinated caudal nerve fibres. (c) Bar graph highlighting the different severity in the reduction of the density of nerve fibres after treatment with either drug. $n = 3$. (d) Box and whiskers plot showing the significant decrease in the density of small unmyelinated intraepidermal fibres after treatment with BTZ but not CFZ. $n = 9$. (e) Representative images of sciatic nerves of untreated control animals and animals treated with BTZ and CFZ. Arrows indicate degenerated fibres. Scale bar: 10 µm. (f) Plot showing the distribution of the diameter of myelinated sciatic nerve fibres. (g) Bar graph highlighting the different severity in the reduction of the density of nerve fibres after treatment with either drug. $n = 3$. Where n=3 experiments, statistical analysis was not carried out, and results should be regarded as preliminary. Data in (b) and (f) are represented as a value distribution. Data in (c) and (g) are represented as mean ± SEM. Data in (d) are represented as box and whiskers, where the box indicates the median value and the interquartile range whereas the whiskers indicate the minimum and maximum values. All groups in (d) were compared using Kruskal–Wallis with Dunn's multiple comparison post hoc test. $^{*}p < 0.05$; $^{**}p < 0.01$. ctrl, control

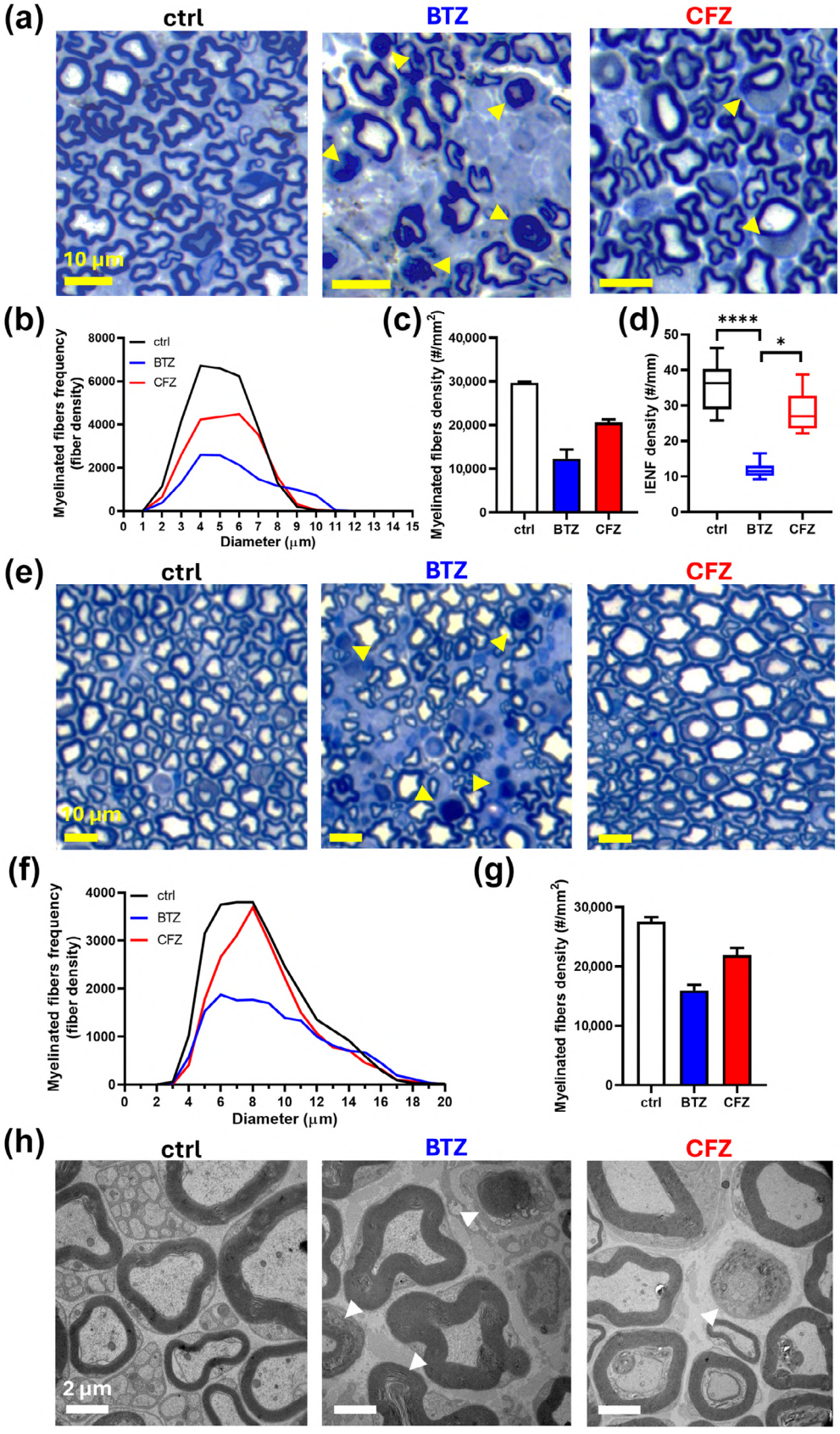

FIGURE 3 Legend on next page.

FIGURE 3 Nerve degeneration caused by carfilzomib (CFZ) is significantly less severe than bortezomib (BTZ) at the end of the treatment cycle. (a) Representative images of caudal nerves of untreated control animals and animals treated with BTZ and CFZ. Arrows indicate degenerated fibres. Scale bar: 10 μm. (b) Plot showing the distribution of the diameter of myelinated caudal nerve fibres. (c) Bar graph highlighting the different severity in the reduction of the density of nerve fibres after treatment with either drug. $n = 3$. (d) Box and whiskers plot showing the significant decrease in the density of small intraepidermal fibres after BTZ treatment. $n = 9$. (e) Representative images of sciatic nerves of untreated control animals and animals treated with BTZ and CFZ. Arrows indicate degenerated fibres. Scale bar: 10 μm. (f) Plot showing the distribution of the diameter of sciatic nerve fibres. (g) Bar graph highlighting the different severity in the reduction of the density of nerve fibres after treatment with either drug. $n = 3$. Where n<5 experiments, statistical analysis was not carried out, and results should be regarded as preliminary. (h) Example TEM images showing fibre ultrastructure in all conditions. Arrows indicate degenerated fibres. Scale bar: 2 μm. Data in (b) and (f) are represented as a value distribution. Data in (c) and (g) are represented as mean ± SEM. Data in (d) are represented as box and whiskers, where the box indicates the median value and the interquartile range whereas the whiskers indicate the minimum and maximum values. All groups in (d) were compared using Kruskal–Wallis with Dunn's multiple comparison post hoc test. $^{*}p < 0.05$; $^{**}p < 0.01$; $^{***}p < 0.001$; $^{****}p < 0.0001$. ctrl, control

end of treatment. When analysing the proteomic data, to select differentially expressed proteins between conditions we set up a significant threshold of 0.01 using the False Discovery Rate (FDR) and a minimum fold-change of 1.5. Proteomic analysis revealed a steep discrepancy in the amount of differentially expressed proteins between the two treatments. After chronic treatment with BTZ 629 proteins were differentially expressed (342 upregulated and 287 downregulated) against control and 179 proteins against CFZ-treated animals (84 upregulated and 93 downregulated) (Figure 4a and Table S1). On the other hand, upon CFZ treatment we only found a total of 12 differentially expressed proteins (11 upregulated and 1 downregulated) versus control (Figure S4 and Table S1). Interestingly, when we compared the list of proteins significantly altered between each treatment, we found a large overlap between the proteins differentially expressed in BTZ versus both CFZ and control samples (66/83 upregulated and 59/93 downregulated), while still having many proteins differentially expressed in BTZ only against control samples (269 upregulated and 227 downregulated) (Figure 4b).

We then proceeded to investigate the identity of the enriched biological processes induced specifically in BTZ-treated samples versus both other conditions by using Gene Ontology (GO) resource (2025-03-16: 40.21) (Ashburner et al., 2000; Gene Ontology Consortium et al., 2023; Thomas et al., 2022) and STRING (v12.0) databases (Szklarczyk et al., 2023). This analysis revealed, among the top pathways referring to proteins that were upregulated in BTZ versus both conditions, a significant enrichment of those involved in the activation and regulation of immune response as well as those activated in response to stress (Figure 4c). Moreover, other enriched pathways refer to axon regeneration, response to axon injury, and neuronal projection development, consistent with the axonopathy profile observed in vivo (Figures 4c and 5a,c[i] and Table S2).

On the other hand, the main pathways enriched within the list of proteins specifically downregulated in BTZ-treated samples referred to axonal transport, mainly along microtubules, and organelle transport and localization, mitochondria in particular (Figures 4C, S5b and 5c[ii]). Indeed, most of the enriched pathways localized mainly within the axon and referred to microtubules and cytoskeletal fibres. Among the many downregulated proteins, of significant importance are many microtubule-interacting proteins that are paramount for microtubule bundle organization such as Tau, MAP 6 and MAP 1B, as well as proteins with a crucial role in axonal transport such as kinesins (KIF5A and 5C), dynactin and dynamin (DCTN1, DNM1), and proteins that regulate axon and axonal initial segment formation and integrity such as TRIM46 and BLOC1S2. Interestingly, we also observed a severe downregulation of all intermediate neurofilaments (NEFL, NEFM and NEFH) that are also crucial regulators of axonal transport and contribute to the maintenance of the axonal calibre, internode length, and conduction velocity (Kriz et al., 2000; Villalón et al., 2018) (Table S3).

In summary, these findings underscore a pronounced difference in the severity of neuropathy caused by the two proteasome inhibitors. Animals treated with BTZ exhibit clear signs of neuropathy as early as halfway through the treatment, with a marked worsening of the phenotype by the end, including severe fibre loss, conduction impairments and mechanical allodynia. Moreover, molecular analyses revealed a profound change in the molecular mechanisms underlying axonal structure and functionality, energy production and intracellular transport. In contrast, CFZ treatment does not induce significant symptoms until the end of the regimen, and even then, the behavioural and morphological effects are notably milder and there are very little changes in protein expression.

3.5 | Carfilzomib (CFZ) treatment does not impair neuron survival or neurite growth in vitro

To establish an in vitro model of BTZ and CFZ treatment on DRG neuronal cells, we assessed the drug concentration that mimicked 80% of proteasome inhibition as detected in the in vivo model and in the clinic setting (Figure 5a). Based on this initial assessment on primary DRG cultures, the doses chosen for BTZ (10 nM) and CFZ (60 nM) were then tested for their efficacy in reducing the viability of a cell line derived from multiple myeloma (RPMI-8226). We found that the efficacy profile of both drugs is very similar; BTZ reduced the percentage of viable cells to 27.17 ± 1.66%, whereas the higher CFZ dose reduced that percentage to 7.10 ± 3.74% (Figure 5b). We further confirmed the drugs' efficacy using an holotomographic microscope with innovative label-free imaging platform (NanoLive SA): We recorded

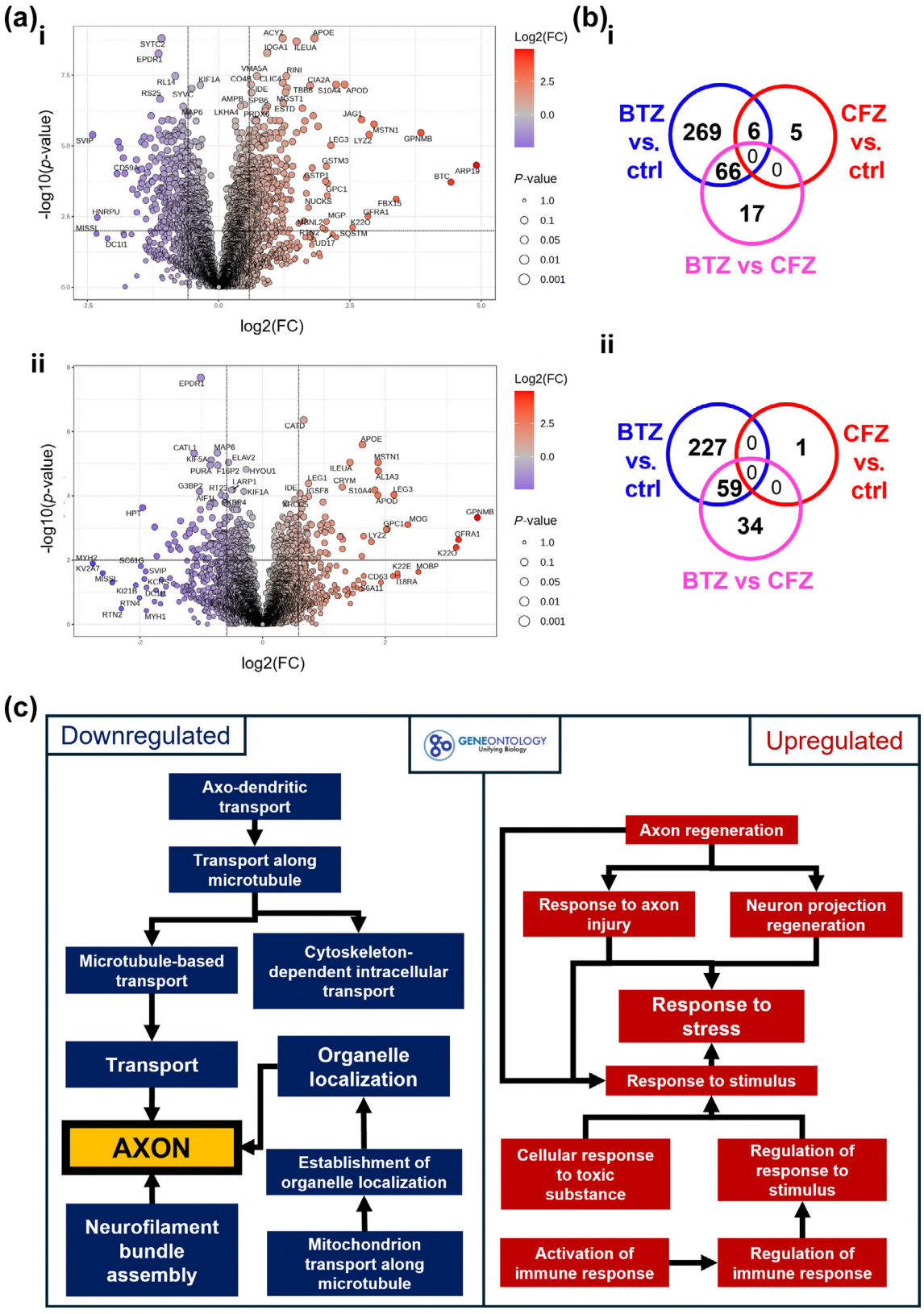

FIGURE 4 Chronic treatment with bortezomib (BTZ) but not carfilzomib (CFZ) significantly alters proteome expression patterns ($n = 6$). (a) Volcano plots showing the differentially expressed proteins between BTZ-treated animals and control (i) or CFZ-treated (ii) animals. FC, fold change. (b) Venn diagrams showing the overlap of upregulated (i) and downregulated (ii) proteins between different conditions. Overview of the top significant ($p < 0.05$ FDR) biological processes resulting from enrichment based on the 59 downregulated (left) and 66 upregulated (right) proteins in BTZ-treated animals versus both CFZ and control (adapted from GO resource: https://geneontology.org/).

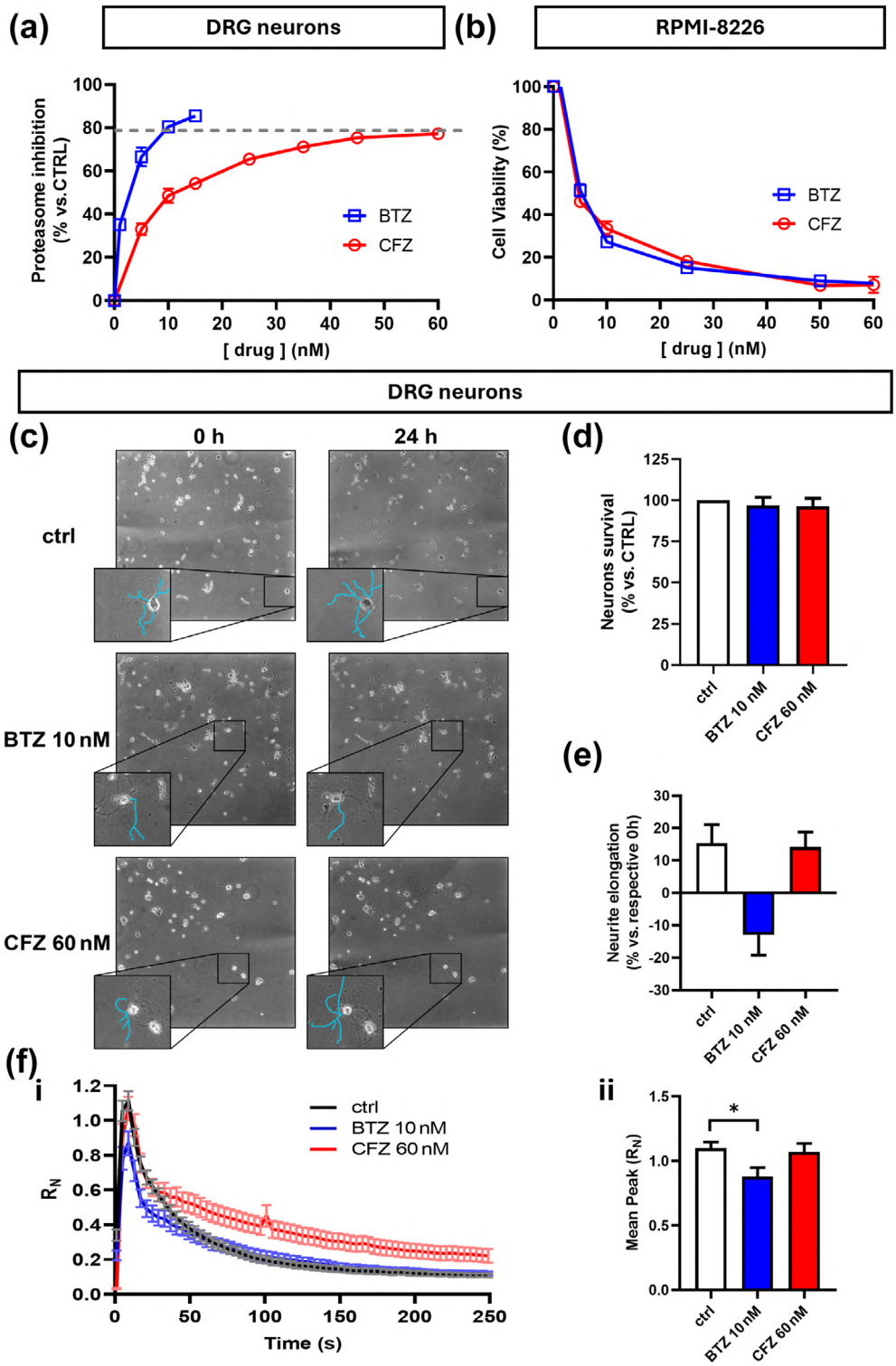

FIGURE 5 Legend on next page.

FIGURE 5 Bortezomib (BTZ) but not carfilzomib (CFZ) reverses neurite elongation in cultured DRG neurons. (a) Plot showing the progressive increase in proteasome inhibition percentage after cultured DRG neurons were treated with increasing doses of BTZ (blue) and CFZ (red), reaching 80% at 10 and 60 nM, respectively. $n = 4$ (ctrl), 3 (BTZ), 2 (CFZ). (b) Plot showing a similar dose-dependent decrease in the viability of RPMI-8226 myeloma cells after treatment with BTZ (blue) and CFZ (red). $n = 6$ (ctrl), 3 (BTZ), 3 (CFZ). (c) Representative images showing neurite elongation in cultured dorsal root ganglion (DRG) neurons after 24 h of treatment with either drug versus control. (d) Bar graph showing the percentage of DRG neuron survival following treatment with either drug, normalized to the control samples. $n = 3$. (f) Bar graph showing negative neurite elongation in DRG neurons following treatment with 10-nM BTZ, an effect not observed in the control or CFZ-treated samples. $n = 3$. Where n<5 experiments, statistical analysis was not carried out, and results should be regarded as preliminary. Ca^{2+} traces plot (i) and mean peak amplitude bar graph (ii) portraying the effect of BTZ and CFZ on KCl-induced (40 mM, 10 s) cytosolic calcium increase in cultured DRG neurons. Note that only BTZ-treated cells displayed a significant reduction of the amplitude of KCl-induced Ca^{2+} transient, whereas CFZ showed a slowed down recovery phase. $n = 66$ (BTZ), 140 (CFZ), 189 (ctrl) cells. Data in (a), (b), and (d–f) are represented as mean ± SEM. All groups in (f)ii were compared using one-way ANOVA with Tukey's multiple comparison post hoc test. Curves in (f)i were compared using a modified Chi-squared test. *$p < 0.05$; **$p < 0.01$; ****$p < 0.0001$. ctrl, control

RPMI-8226 cells for 24 h and observed a mortality of at least 80% for both drugs, as well as an increasing tendency towards necrosis as cellular death mechanism (Figure S6 and Movies S1–S3). Next, the neurotoxicity profile of the drugs was assessed on primary DRG neuron cultures: none of the drugs impacted on neuronal survival after 24 h (Figure 5c,d). However, only BTZ clearly affected neurite elongation, whereas CFZ did not show any sign of neurite growth impairment (−12.98% ± 6.21% BTZ vs. 15.98% ± 5.78% ctrl vs. 15.15% ± 4.61% CFZ) (Figure 5e). When looking at the functional response of neurons to a depolarizing stimulus (TS with 40-mM KCl, 10 s) in terms of modulation of cytosolic Ca^{2+} signals BTZ, but not CFZ, significantly reduced KCl-induced peak of cytosolic calcium transient after 24 h of treatment, as assessed using cytosol-located Fura-2 probe (Figure 5f). However, CFZ impacts the recovery phase of the cytosolic calcium (X^2 test, $p < 0.001$), suggesting that the drug alters the neuronal calcium homeostasis.

3.6 | Bortezomib (BTZ) but not carfilzomib (CFZ) promotes microtubule hyper-stabilization 10-h post-treatment

We aimed to dissect the temporal course of the molecular events leading to neurotoxicity to identify any difference between the two drugs and highlight the best time window to maximize the efficacy of any protective treatment. For this reason, all the subsequent assays were performed following either 10 or 24 h of treatment.

Given the significant impact of BTZ on neurite elongation, as well as its off-target specific binding to tubulin, we assessed any change in the level of selected tubulin PTMs associated with microtubule stability, as well as the expression of microtubule-associated proteins, that could alter microtubule stability leading to axonal degeneration (Malacrida et al., 2021). Immuno-fluorescence analyses of cultured DRG neurons revealed that BTZ elicited a significant increase in the presence of Δ2-tubulin with respect to the total levels of β3-tubulin as early as 10 hours after treatment (Figure 6a[i],b[i]), that consolidated over time (Figure 6a[i],c[i]). Treatment with CFZ does not change the levels of Δ2-tubulin at any point during treatment (Figure 6a[ii],b[i],c[i]). Correspondingly, we observed an increased number of fragmented axons with the presence of varicosities (Figure 6a) reminiscent of axonal degeneration; the degeneration index (see Section 2) was significantly higher in cells treated with BTZ than in all other conditions after 10 h of treatment (Figure 6b[ii]). CFZ, however, induced slight degeneration at 10 h (Figure 6b[ii]), that increased slowly over time to reach BTZ levels after 24 h of treatment (Figure 6c[ii]).

Similarly, when we measured the expression levels of two different PTMs of tubulin (Δ2, acetylation) that associate with long-lived microtubules, only BTZ induced a substantial accumulation of both (Figure 6d,e), as well as MAP 2, a microtubule-associated protein (Figure 6f). The increase in Δ2-tubulin and MAP 2 and its timing confirmed the previous observations on cultured DRG neurons (Figure 6d[i],f[i]) and was even more evident after 24 h, with an increase to over 200% compared to control values (Figure 6d[ii],f[ii]). Conversely, CFZ showed no significant change in either tubulin PTM or MAP 2, with expression levels comparable to control ones.

The accumulation of Δ2-tubulin confirms the specific effect of BTZ on microtubule hyper-stabilization that is absent upon CFZ treatment and is coincidental with the earlier onset of axonal degeneration observed with BTZ.

3.7 | Both bortezomib (BTZ) and carfilzomib (CFZ) induce alterations in mitochondria morphology and bioenergetics

Mitochondria are organized in a continuously remodelling network, regulated by a constant cycle of fusion and fission events, which influences cell functionality beyond energy production (Stanga et al., 2020; Tábara et al., 2025). Proteasome inhibitors are thought to target mitochondria, altering not only their functionality, but their morphology and dynamics as well, all mechanisms that may contribute to CIPN induction. By means of the Mitochondrial Network Analysis (MiNA), we found that both BTZ and CFZ treatments affect the morphology of mitochondria as well as their organization within cultured DRGs that were stained with TOM20 after 24 h of treatment (Figure 7a). Indeed, whereas the area occupied by mitochondria remained overall unchanged (Figure 7b), MiNA revealed

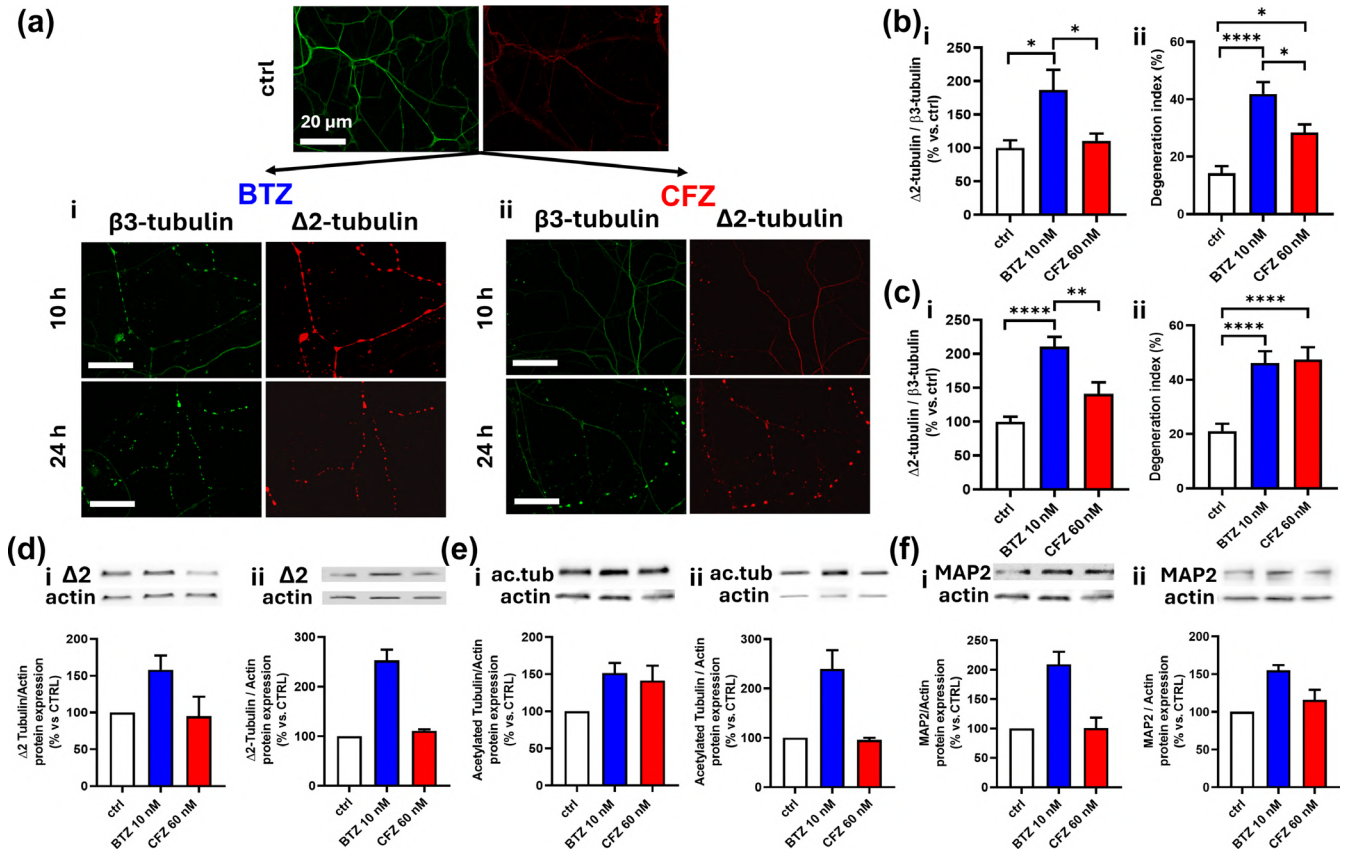

FIGURE 6 Bortezomib (BTZ), but not carfilzomib (CFZ), induces stable tubulin PTMs expression and early axonal degeneration after 10 h of treatment in cultured DRG neurons. (a) Representative IF images of β3- (green) and Δ2-tubulin (red) staining in axons of cultured dorsal root ganglion (DRG) neurons treated with 10-nM BTZ (i) and 60 nM of CFZ (ii) for the indicated times. (b) Bar graphs showing the ratio between the intensity of Δ2- and β3-tubulin (i), as well as the axonal degeneration index (ii) in cultured DRG neurons treated with both drugs for 10 h. Data in (i) are normalized to control values. $n = 19$ (ctrl), 22 (BTZ), 21 (CFZ) areas in Bi; $n = 20$ (ctrl), 23 (BTZ), 20 (CFZ) areas in Bii. (c) Bar graphs showing the ratio between the intensity of Δ2- and β3-tubulin (i), as well as the axonal degeneration index (ii) in cultured DRG neurons treated with both drugs for 24 h. Data in (i) are normalized to control values. $n = 19$ (ctrl), 21 (BTZ), 13 (CFZ) areas in Ci; $n = 21$ (ctrl), 21 (BTZ), 15 (CFZ) areas in Cii. (d) Bar graphs showing expression levels of Δ2-tubulin after 10 h (i) or 24 h (ii) of treatment with either drug. $n = 3$. (e) Bar graphs showing expression levels of acetylated tubulin after 10 h (i) or 24 h (ii) of treatment with either drug. $n = 3$. (f) Bar graphs showing expression levels of MAP 2 after 10 h (i) or 24 h (ii) of treatment with either drug. All expression levels in (d–f) are normalized to the control values. $n = 3$. Where n<5 experiments, statistical analysis was not carried out, and results should be regarded as preliminary. Data in all panels are represented as mean ± SEM. As n=3 for these experiments, statistical analysis was not carried out, and results should be regarded as preliminary. Data in (b) and (c) were compared using one-way ANOVA with Tukey's multiple comparison post hoc test. *$p < 0.05$; **$p < 0.01$; ****$p < 0.0001$. ctrl, control

fragmentation of the mitochondrial network, highlighted by an increase in the number of individual mitochondria and by the number of multiple networks after treatment with BTZ and CFZ compared to control samples (Figure 7c,d). Interestingly, when analysing multiple parameters referring to the complexity of the networks and branches, we found that the number of end-point and junction voxels were reduced only after treatment with BTZ indicating that in this condition, compared to CFZ and control, there was a significantly decreased network complexity (Figure 7e,f). The number of slab voxels was consistently low albeit non-significant after treatment with both drugs, indicating shorter branches (Figure 7g).

Indeed, treatment with either drug led to a substantial decrease in mitochondrial respiratory capacity (Figure 8a). As measured by the Seahorse Assay, both basal and maximal oxygen consumption rates, as well as ATP production, were reduced to 50% of normalized control levels after 24 h of treatment. Moreover, both drugs significantly reduced the peak of KCl-induced (TS with 40-mM KCl, 10 s) Ca^{2+} transients in the mitochondrial matrix, assessed using mt-fura-2.3, a mitochondria-targeted variant of Fura-2 probe (de Nadai et al., 2021; Pendin et al., 2019), suggesting an impairment of mitochondrial activity and intra-organelle Ca^{2+} homeostasis (Figure 8b).

The mitochondrial membrane potential is another essential component in the process of energy storage and ATP production. Treatment with either drug induced significant depolarisation of the mitochondrial membrane as early as 10 h after treatment, remaining stable at the 24-h time point (Figure 8c–e). Moreover, either treatment induced a decrease in the expression of the voltage-gated mitochondrial cationic channel Voltage Dependent Anion Channel (VDAC) down to approximately 50% of control levels after 24 h (Figure 8f).

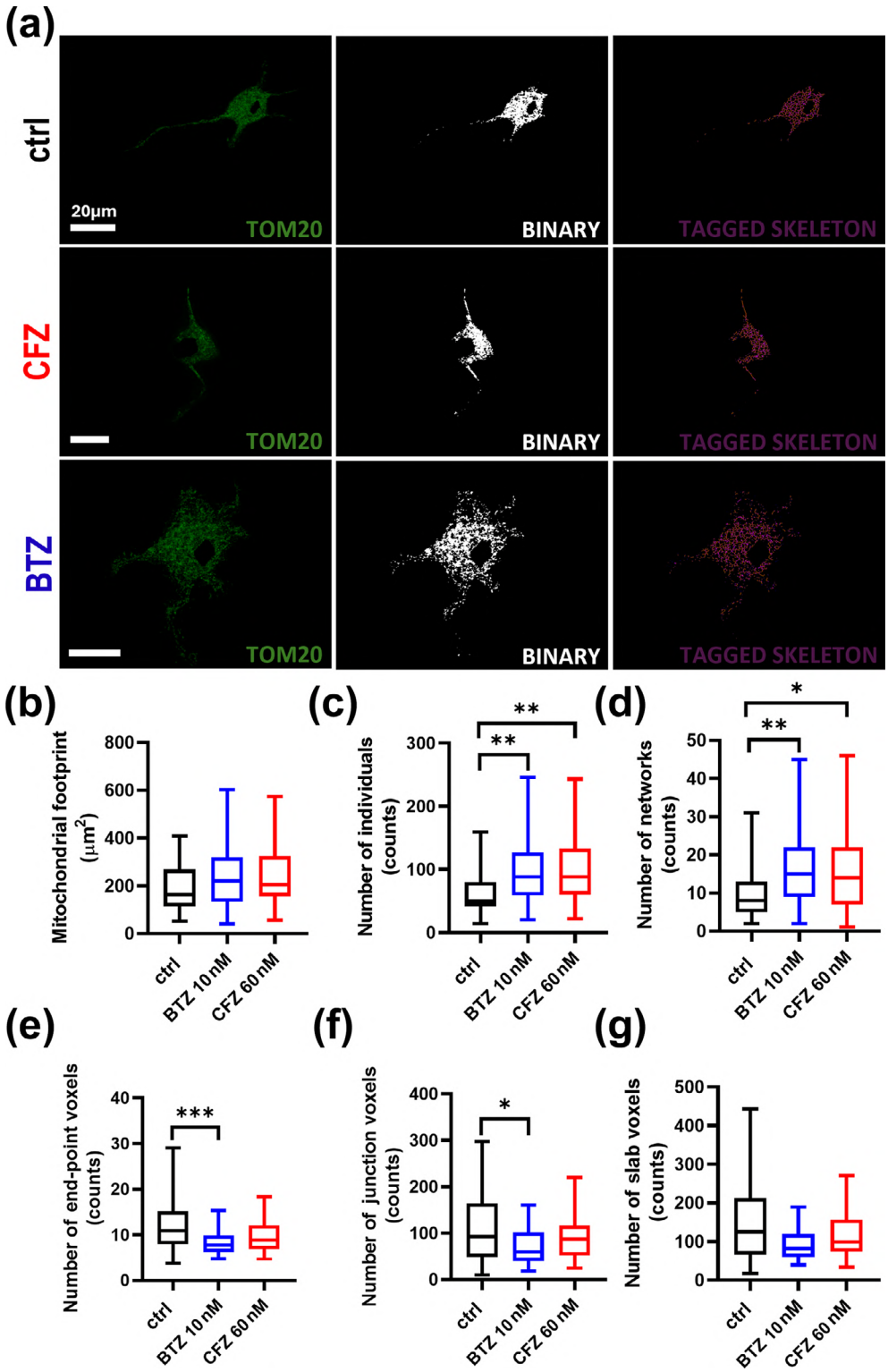

FIGURE 7 Bortezomib (BTZ) and carfilzomib (CFZ) differentially affect the morphology of the mitochondrial network organization in cultured dorsal root ganglion (DRG) neurons. (a) Representative images showing the staining of mitochondria (TOM20, green) and the respective binary and skeletonized images in control condition and treated with BTZ or CFZ. The scale bar in all images is 20 µm. (b–g) Bar graphs showing the mitochondrial footprint (b), the number of individual mitochondria (c), the number of networks (d), the number of end-point voxels (e), the number of junction voxels (f) and the number of slab voxels (g) after 24 h of treatment with either drug. $n = 39$(ctrl), 45 (BTZ), 42 (CFZ) cells. Data from (b) to (g) are represented as box and whiskers, where the box indicates the median value and the interquartile range whereas the whiskers indicate the minimum and maximum values. All groups were compared using Kruskal–Wallis test with Dunn's multiple comparison post hoc test. $^{*}p < 0.05$, $^{**}p < 0.01$, $^{***}p < 0.001$. ctrl, control

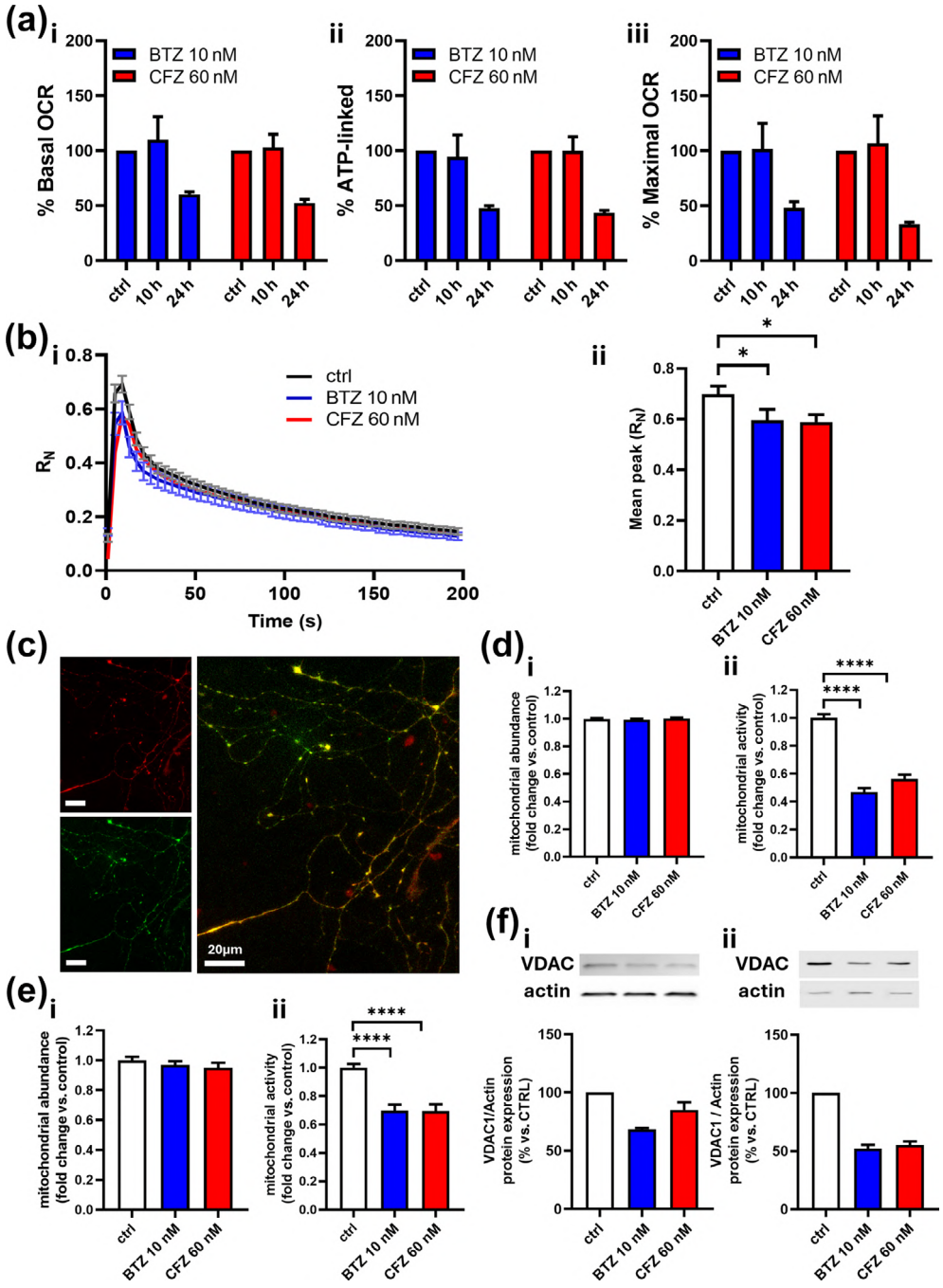

FIGURE 8 Bortezomib (BTZ) and carfilzomib (CFZ) impair mitochondrial function and membrane ion channels expression in cultured dorsal root ganglion (DRG) neurons. (a) Bar graphs showing the decrease in the levels of basal (i), ATP-linked (ii) and maximal oxygen consumption rate (OCR) (iii) over time after treatment with BTZ (blue) and CFZ (red). $n = 3$. (b) Ca^{2+} traces (i) portraying the effect of KCl-induced mitochondrial calcium increases, measured using mt-fura-2.3, showed how neuronal cells treated with both drugs displayed a significant decrease in the peak amplitude (ii). $n = 189$ (ctrl), 66 (BTZ), 140 (CFZ) cells. (c) Representative images showing neurites stained with MitoTracker TM Red CMXRos (top left) and MitoTracker TM Green FM (bottom left) as well as the merged image (right). (d) Bar graphs showing the changes in mitochondrial abundance (i) and activity (ii) after 10 h of treatment with either drug. $n = 5$. (e) Bar graphs showing the changes in mitochondrial abundance (i) and activity (ii) after 24 h of treatment with either drug. All data in (e) and (f) are normalized to control values. $n = 5$. (f) Bar graphs comparing the expression levels of VDAC1 after 10 h (i) or 24 h (ii) of treatment with either drug, normalized to control values. $n = 3$. Where n<5 experiments, statistical analysis was not carried out, and results should be regarded as preliminary. Data in (a), (b) and (d–f) are represented as mean ± SEM. All groups in (b)ii, (d) and (e) were compared using one-way ANOVA with Tukey's multiple comparison post hoc test. Curves in (b)i were compared using a modified Chi-squared test. *$p < 0.05$, **$p < 0.01$; ***$p < 0.001$; ****$p < 0.0001$. ctrl, control

Altogether, these findings highlight the impact of the two drugs on both mitochondrial structure and function, starting by affecting some mitochondrial dynamics at 10 h and becoming more severe following 24 h of treatment, with an impairment of the capability of mitochondria to organize structurally and produce energy as a consequence.

3.8 | Bortezomib (BTZ) but not carfilzomib (CFZ) impairs mitochondrial trafficking and increases the fraction of stationary mitochondria

Mitochondrial trafficking is paramount for correct cellular function. Due to their complex geometry and long extensions, neurons are severely impacted by any defect in the transport of cargos along the microtubules (Schwarz, 2013). Moreover, we already observed a significant downregulation of several proteins involved in microtubule-based axonal transport in vivo specifically after chronic treatment with BTZ (Figures 4 and S5).

Analysis of axonal mitochondrial motility following treatment strikingly revealed that only BTZ significantly affected mitochondrial motility within the axons (Figures 9a–d and S7). In fact, 24 h after treatment, BTZ significantly reduces the overall motility of mitochondria, reducing both anterograde and retrograde moving ones to less than 50% of control values. Moreover, we observed a steep increase in the percentage of stationary mitochondria to more than 200% of control values (Figure 9b).

Taken together, these results show an important difference between CFZ and BTZ in their effects on mitochondrial trafficking, with BTZ significantly impacting motility along the axon, presumably because of its specific effects on cytoskeleton organization.

4 | DISCUSSION

Proteasome inhibitors induce CIPN as one of their main side effects. Currently, no therapeutic strategy has proven to be effective: The possibility to develop better treatment solutions for this condition is

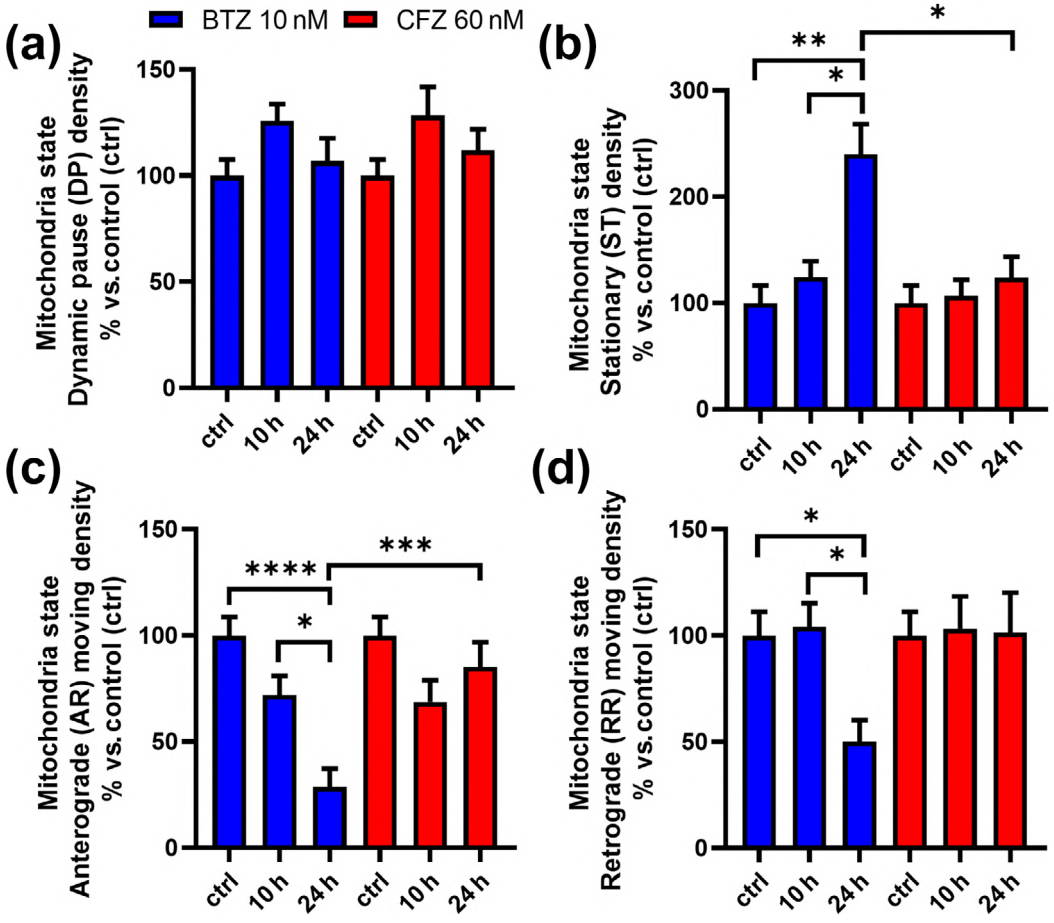

FIGURE 9 Only carfilzomib (CFZ) significantly impaired mitochondrial motility after 24 hours of treatment in cultured dorsal root ganglion (DRG) neurons. (a–d) Bar graphs showing the proportion of mitochondria having different kinds of motility behaviour before and after treatment with bortezomib (BTZ) (blue) or CFZ (red): dynamic pause (DP) (a), stationary (ST) (b), anterograde moving (AR) (c) or retrograde moving (RR) (d). $n = 11$ (ctrl), 14 (BTZ), 15 (CFZ) axons. Data in all panels are represented as mean ± SEM. All groups were compared using one-way ANOVA (a, c) or ANOVA with Brown–Forsythe and Welch corrections (b, d), with Sidak's (a, c) or Tamahane's (b, d) multiple comparison post hoc tests. $^{*}p < 0.05$, $^{**}p < 0.01$; $^{***}p < 0.001$; $^{****}p < 0.0001$. ctrl, control

locked behind the need to understand the specific molecular mechanisms underlying the development of neuropathy.

In the present work, we have compared two different proteasome inhibitors, BTZ and CFZ, that present different neurotoxicity profiles in clinical practice by developing a novel mouse model of CFZ-induced neuropathy to be compared to a well-established BTZ-induced one (Carozzi et al., 2010, 2013; Carozzi, Chiorazzi, et al., 2015; Cavaletti et al., 2007). The significant decrease in potential amplitude and conduction velocity in caudal nerves, as well as the development of mechanical allodynia correlated with significant loss of both small intraepidermal fibres and large myelinated fibres in BTZ-treated mice, indicate clear signs of peripheral axonopathy and recapitulate what has been previously described (Bruna et al., 2010; Carozzi et al., 2013; Meregalli et al., 2010). On the other hand, a preclinical model of CFZ-induced CIPN had not been developed until now, although evaluation of its antineoplastic efficacy had been performed previously (Demo et al., 2007; Kuhn et al., 2007). Here, we used a chronic treatment schedule that consisted of two consecutive days of intravenous injection of CFZ, similarly to a standard clinical regimen, over 4 weeks (Shah et al., 2018), using a drug concentration able to induce a degree of proteasome inhibition similar to BTZ. The in vivo characterization of our model revealed an axonopathy of reduced severity and delayed onset compared to BTZ-treated animals, because some evidence of degeneration appeared only at the end of the treatment. This difference in terms of incidence of neurotoxicity and severity is largely consistent with previous clinical studies (Groen et al., 2019; Peng et al., 2015). Indeed, reports from multiple Phase I/II clinical trials illustrate how CFZ patients did not report peripheral neuropathy of Grade 3 or above, which is one of the main side effects of BTZ therapy that necessitates immediate treatment discontinuation (Strifler & Knop, 2018; Yang, Zhao, et al., 2024). Moreover, a recent meta-analysis of 13 CFZ-based trials stated that 21% of patients reported peripheral neuropathy symptoms, with only 1% at Grade 3, whereas a recent review of phase III clinical trials stated that patients treated with BTZ report CIPN in 37.8% of cases and 8% report severe neuropathy at or above Grade 3 (Li et al., 2020; Sheng et al., 2017; Yee, 2021). Moreover, because CFZ has been approved for both relapse and refractory multiple myeloma (MM), often patients have existing peripheral neuropathy due to previous treatment with BTZ or thalidomide: however, CFZ-treated patients reported low adverse effects due to neuropathic symptoms, and again rarely at Grade 3 (Siegel et al., 2013). Because a precise pathogenesis of CIPN has not been fully elucidated, there are currently no highly recommended preventive or therapeutic approaches: current clinical practice focusses on relieving the sensory symptoms, pain in particular, through the use of analgesic and antiallodynic drugs (Wen et al., 2023; Yang, Zhao, et al., 2024). Among many analgesic drugs tested in randomized control trials or preclinical studies, pregabalin attenuated mechanical allodynia in CIPN rats treated with BTZ and is the most commonly used analgesic drug in clinical practice (Yamamoto et al., 2015). Moreover, neuroprotective strategies like antioxidant therapies or targeting glial dysfunction have been proven mildly effective in preclinical studies (Callander et al., 2014; Robinson et al., 2014; Yang, Zhao, et al., 2024).

However, none of the illustrated treatment paradigms have been proven to be highly efficient: therefore, a paramount step in developing a bespoke therapeutic intervention to ameliorate CIPN symptoms is the investigation and identification of any altered molecular mechanisms that are specific for each drug.

Many recent studies suggest that BTZ neurotoxicity is strongly related to microtubule polymerization and hyper-stabilization that could drive axonal degeneration (Meregalli et al., 2014; Poruchynsky et al., 2008; Staff et al., 2013). These mechanisms are thought to be a consequence of off-target binding of BTZ to tubulin as reported by a recent study performed by Malacrida and colleagues, in which a SPILLO-PBSS analysis of BTZ and CFZ has identified tubulin as a top 10 binding target of BTZ but not of CFZ, as well as a specific increase of polymerized GTP-bound tubulin induced by BTZ (Malacrida et al., 2021).

Indeed, our analysis of the proteome showed very few changes in the DRG collected from CFZ-treated mice versus control samples, with no clear indication of a role for any specific pathway or biological process. On the contrary, BTZ-treated animals showed deregulation of several cellular pathways that play a crucial role in cell homeostasis. When dissecting upregulated proteins, the main enriched pathways were involved in activation of immune response and response to stress, as well as response to axonal injury and regeneration. Furthermore, when analysing downregulated protein pathways, we observed a significant enrichment of many molecules and pathways that are crucial for correct axonal function, like transport of proteins and organelles along microtubules as well as maintenance of the axon's calibre and structural integrity. Many proteins that interact with microtubules as well as molecular motors and other cytoskeletal proteins are specifically affected by BTZ treatment, because they were found also to be significantly downregulated versus CFZ-treated animals. The striking difference between the strong dysregulation observed upon BTZ treatment and the few changes upon CFZ administration reveals a much stronger impact of BTZ on inflammation, immune and stress response, and cellular ultrastructure. Their shared effect on proteasome inhibition cannot explain this difference, because in recent studies only BTZ—but not CFZ or other PIs—induced **Cav3.2** calcium channel increase and reduced neurite outgrowth with comparable proteasome inhibition (Arastu-Kapur et al., 2011; Tomita et al., 2019; Yang, Zhao, et al., 2024). This in-depth analysis of BTZ and CFZ-dependent CIPN-related proteome changes is a clear novelty in terms of clinical translation firstly because it employs the first developed preclinical model of CFZ-dependent CIPN. Moreover, previous analyses were mostly performed in vitro on myeloid cell lines and were dedicated to analysing protein level changes upon anti-tumour treatment to correlate the proteome profile to tumoural drug resistance (Han et al., 2024; Porras-Yakushi et al., 2021). Some insights on neurotoxicity mechanisms were reported by Karademir et al. (2018), who however did not use a chronic treatment animal model but nonetheless showed a downregulation of microtubule-associated proteins on neural stem cells isolated in vitro from mouse embryos after 24 h of treatment with BTZ but not CFZ. This study corroborates our results and delineates a much

milder impact of CFZ treatment on many different cellular pathways, from microtubule but also actin cytoskeleton to assisted protein folding, endoplasmatic reticulum (ER)-associated protein degradation, as well as the antioxidant systems. This differential impact of the two drugs therefore does not seem to depend on PIs' main mechanism of action but may arise from specific off-target effects of BTZ.

To better characterize the initiating events correlated with the onset of peripheral neuropathy, we investigated antitumour activity and neurotoxicity in vitro, using tumour cell lines and cultured DRG neurons. Cellular viability in multiple myeloma showed that at the chosen doses BTZ reduced survival of RPMI8226 cells to less than 30% and CFZ to about 10%, respectively. In addition, none of the drugs induced a significant reduction in neuronal survival, but only BTZ reversed neurite elongation from +15% of control samples to −13% after 24 h of treatment. Interestingly, Wolf et al. (2010) reported a 40% reduction in neurite length in SH-SY5Y cells after 24 h of treatment with 10 nM of BTZ, with respect to CFZ- or vehicle- treated cells. Moreover, Staff et al. (2013) and Snavely et al. (2022) observed a dose-dependent reduction in neurite outgrowth but not survival rate treating rat DRG neuron explants and human-derived sensory neurons with varying concentrations of BTZ, respectively. When treatment times expanded to 48 h, BTZ, but not CFZ, also showed an effect on neuronal survival accentuating its different toxicity profile (Malacrida et al., 2021). We then proceeded to investigate potential mechanisms of neurotoxicity related mainly to alterations in the microtubule cytoskeleton and mitochondria structure, function and trafficking, to discern between shared and specific mechanisms and precisely dissect their onset to unveil potential temporal correlations.

4.1 | Calcium and mitochondrial homeostasis defects are neurotoxicity mechanisms shared by both proteasome inhibitors

Altered calcium homeostasis has been implicated as a mechanism for cell suffering and death in many neurodegenerative diseases (Betzer & Jensen, 2018), as well as a key player in CIPN induced by many different chemotherapy drugs, influencing membrane excitability, neurotransmitter release and gene expression (Carozzi, Canta, & Chiorazzi, 2015; Starobova & Vetter, 2017).

We observed a significant impact of both drugs on cytosolic and mitochondrial calcium levels. Our analysis of the cytosolic calcium peaks revealed a decrease in calcium transients' amplitude only with BTZ, whereas CFZ impacts the recovery phase, suggesting the presence of different molecular mechanisms that drive a similar effect on calcium homeostasis. Mitochondrial calcium peaks decreased in a similar fashion after treatment with both drugs, indicating an alteration in calcium level regulation induced by mitochondrial dysfunction.

Indeed, recent studies show that chemotherapeutic agents disrupt mitochondrial structure and bioenergetics, increase nitro-oxidative stress and alter mitochondrial transport, fission, fusion and mitophagy also through impairment of their interaction with cytoskeletal proteins (Doyle & Salvemini, 2021; Smith et al., 2016). Using the MiNA tool, we showed that both drugs significantly alter mitochondrial morphology and network organization after 24 h from treatment. Interestingly, BTZ decreased network complexity and increased fragmentation more than CFZ. Our findings expand the information previously reported of a similar effect of 100 nM of BTZ and CFZ where an increase in the number of individual mitochondria as well as decrease in the number of branches after 24 h of treatment was observed (Jannuzzi et al., 2020).

These morphological alterations mirror the observed decrease in mitochondrial functionality: Indeed, 10 h of treatment with both drugs significantly impaired the mitochondrial membrane potential, whereas at 24 h, also, respiratory capacity was significantly reduced to less than 50% of control values. Calcium dysregulation and subsequent caspase activation is a critical determinant of BTZ cytotoxicity in myeloma cells (Landowski et al., 2005). We found such dysregulation in cultured neuronal cells correlated with a clear impact on mitochondrial activity, calcium homeostasis, ion channels expression and energy production. Previous reports showed a similar alteration in mitochondrial membrane potential and respiratory capacity both in vitro and in vivo following BTZ but not CFZ treatment (Janes et al., 2013; Jannuzzi et al., 2020; Maharjan et al., 2014; Snavely et al., 2022; Zheng et al., 2012).

4.2 | Cytoskeletal and mitochondrial trafficking impairments are BTZ-specific mechanisms of neurotoxicity

When investigating cytoskeletal alterations that related specifically to microtubules, however, we observed a very different impact of the two drugs.

We detected a clear difference in the levels of tubulin PTMs related to microtubule stabilization (Δ2 and acetylation), with BTZ inducing a marked accumulation of Δ2-tubulin as early as 10 h after treatment, and of both PTMs after 24 h. These data suggest that early microtubule hyper-stabilization drives early axonal degeneration in neurons treated with BTZ, whereas CFZ-treated neurons, in which no difference in tubulin PTMs was observed, do not degenerate until later. The pathogenic increase in Δ2-tubulin driving axonal degeneration has been previously reported with a higher dose of BTZ (100 nM) and demonstrated as a starting point for BTZ-induced axonal degeneration (Pero et al., 2021). The increase in tubulin acetylation is more controversial, because there are both reports of an increase in acetylated tubulin in HCN-1A and HCN-2 neuronal cell lines following treatment with BTZ, and of axonal degeneration and increase in tubulin polymerization independent from tubulin acetylation in a model of ex vivo rat DRG neurons (Poruchynsky et al., 2008; Staff et al., 2013).

In our study, we observed a substantial increase in MAP 2 expression in neurons treated with BTZ as early as 10 h after treatment, similarly to a previous work in BTZ-treated HCN-2 neuronal cell lines (Poruchynsky et al., 2008). Our proteomic data, however, also show a significant decrease in several other microtubule-interacting proteins

such as MAP 6, MAP 1B and Tau. These apparent discrepancies may result in a profound deregulation of microtubule dynamics with dramatic consequences on axonal transport. An excess in MAP 2 may contribute to axonal transport inhibition by competing with kinesins and dyneins for tubulin binding (Dehmelt & Halpain, 2005). On the other hand, loss of MAP 6 might affect microtubule structure and reduce microtubule resistance to mechanical stress (Cuveillier et al., 2020). Moreover, reduced levels in MAP 1B and Tau may both contribute to loss of axonal outgrowth and/or regeneration (Dehmelt & Halpain, 2005). We can speculate that the simultaneous increase in MAP 2 and tubulin PTMs, together with a loss of microtubule-associated proteins like MAP 1B and Tau may explain the pleiotropic damage inflicted by chronic administration of BTZ on axonal transport and microtubule structural integrity bringing forth axonopathy and nerve degeneration.

Because mitochondria in the peripheral nervous system are mainly located within the axons, their transport and its interplay with axonal energy homeostasis are fundamental for correct cellular function: Any alteration in either of these mechanisms can cause neurotoxicity (Pero et al., 2021; Sheng, 2017; Staff et al., 2013; Yan et al., 2021). In this study, we observed that CFZ treatment had no significant effect on mitochondrial motility, whereas BTZ, after 24 h of treatment, showed a massive decrease in both anterograde and retrograde motion, to levels less than 50% of control, as well as a doubling of stationary mitochondria. Similar effects of BTZ on axonal transport and mitochondrial movement, velocity and distance travelled have been replicated in mouse, rat and human-derived sensory neurons (Alé et al., 2015; Hrstka et al., 2021; Pero et al., 2021; Staff et al., 2013). These results correlated well with the observed effect on microtubule hyper-stabilization in vitro and with the downregulation of various proteins involved in axonal transport and organelle motility observed after a chronic treatment regimen.

CONCLUSIONS

This multidisciplinary study on proteasome inhibitors-dependent neurotoxicity provides new and solid evidence on the specific molecular mechanisms of action of BTZ and CFZ. Our results highlighted a clear difference in the neurotoxicity profile between the two drugs, with BTZ-treated animals exhibiting stronger and earlier neurotoxic symptoms that correlated with loss of fibres already at mid-treatment and extensive protein expression changes. These differences recapitulated in vitro, where BTZ impaired neurite extension and drove early axonal degeneration while impacting on tubulin PTMs levels, a specific effect on microtubules. These early alterations correlated with profound inhibition of axonal mitochondrial transport, a mechanism mirrored by significant downregulation of protein implicated in microtubule-based transport and axonal integrity observed in vivo.

Taken as a whole, these results strengthen our understanding of the neurotoxicity caused by BTZ compared to CFZ and provide a much-needed, clear timing of the onset of perturbations, paving the way for tailored therapeutic strategies to reduce CIPN symptoms and ameliorate the condition of cancer patients undergoing such treatments.

AUTHOR CONTRIBUTIONS

Federico Iseppon: Conceptualization; investigation; methodology; data curation; writing—review and editing; writing—original draft; visualization; validation; formal analysis. **Alessio Malacrida:** Conceptualization; investigation; writing—review and editing; writing—original draft; methodology; data curation; validation; formal analysis; visualization. **Alessia Chiorazzi:** Investigation; methodology; writing—review and editing. **Annalisa Canta:** Investigation; methodology; writing—review and editing. **Paola Alberti:** Investigation; methodology; writing—review and editing. **Valentina Alda Carozzi:** Investigation; methodology; writing—review and editing. **Eleonora Pozzi:** Investigation; methodology; writing—review and editing. **Virginia Rodriguez-Menendez:** Investigation; methodology; writing—review and editing; visualization; formal analysis. **Laura Cherchi:** Investigation; methodology; writing—review and editing. **Valentina Fabbro:** Investigation; methodology; data curation; writing—review and editing. **Lisa Pagani:** Investigation; methodology; writing—review and editing; formal analysis. **Elisa Tonelli:** Investigation; methodology; writing—review and editing. **Laura Tapella:** Investigation; methodology; writing—review and editing; formal analysis. **Andrea Mattarei:** Resources; writing—review and editing. **Sara Palermo:** Investigation; methodology; writing—review and editing. **Daniele Cartelli:** Investigation; methodology; data curation; visualization; writing—review and editing; formal analysis. **Mario Mauri:** Investigation; methodology; visualization; writing—review and editing; formal analysis. **Noemi Scimia:** Investigation; methodology; writing—review and editing. **Serena Stanga:** Investigation; methodology; writing—review and editing; visualization; formal analysis. **Dmitry Lim:** Writing—review and editing; methodology. **Carla Distasi:** Writing—review and editing; methodology. **Marta Delconti:** Investigation; methodology; writing—review and editing. **Clizia Chinello:** Methodology; investigation; writing—review and editing. **Patricia Morcillo:** Investigation; methodology; writing—review and editing. **Maria Elena Pero:** Investigation; methodology; writing—review and editing; visualization; data curation; formal analysis. **Francesca Bartolini:** Writing—review and editing. **Guido Cavaletti:** Conceptualization; writing—review and editing; supervision. **Cristina Meregalli:** Project administration; resources; supervision; conceptualization; writing—original draft; writing—review and editing; funding acquisition.

AFFILIATIONS

[1]Experimental Neurology Unit, School of Medicine and Surgery, University of Milano-Bicocca, Monza, Italy

[2]Fondazione IRCCS San Gerardo dei Tintori, Monza, Italy

[3]Proteomics and Metabolomics Unit, School of Medicine and Surgery, University of Milano-Bicocca, Vedano al Lambro, Italy

[4]Department of Pharmaceutical Sciences, Università del Piemonte Orientale, Novara, Italy

[5]Department of Pharmaceutical and Pharmacological Sciences, University of Padua, Padua, Italy
[6]Department of Biosciences, Università degli Studi di Milano, Milan, Italy
[7]Neuroalgology Unit, Fondazione IRCCS Istituto Neurologico Carlo Besta, Milan, Italy
[8]School of Medicine and Surgery, University of Milano-Bicocca, Monza, Italy
[9]Neuroscience Institute Cavalieri Ottolenghi, Department of Neuroscience Rita Levi Montalcini, University of Turin, Turin, Italy
[10]Department of Pathology and Cell Biology, Columbia University, New York, New York, USA
[11]Department of Veterinary Medicine and Animal Production, University of Naples Federico II, Naples, Italy

ACKNOWLEDGEMENTS

This study is part of the project PRIN 2022 PNRR with Code P2022R43RA (Ministero dell'Istruzione, dell'Università e della Ricerca), which has received funding from NextGeneration EU – MUR – M4C2 1.1 (CUP C53D2300850000). This work is also supported by Fondo Unico degli Investimenti (FUI 2023) – Fondi di Ateneo UPO-DISS, DIMET, DSF. This work is also supported by Fondazione Cariplo (Grant # 2019-1482) and R01CA279401A1 (NIH/NCI) and RF1AG050658 (NIH/NIA) to F.B. The authors would like to thank Prof. Nicolini for her valuable guidance. The expert technical support of Dr.ssa Fantoni, Dr.ssa Ballarini and Dr. Mario Bossi in the preparation of the samples used for pathological investigation is gratefully acknowledged by the authors. In addition, PI is extremely grateful to Prof. Rumora and Prof. Feldman for mitochondrial trafficking training. Open access publishing facilitated by Universita degli Studi di Milano-Bicocca, as part of the Wiley - CRUI-CARE agreement.

CONFLICT OF INTEREST STATEMENT

The authors declare no conflicts of interest.

DECLARATION OF TRANSPARENCY AND SCIENTIFIC RIGOUR

This Declaration acknowledges that this paper adheres to the principles for transparent reporting and scientific rigour of preclinical research as stated in the BJP guidelines for Design and Analysis, Immunoblotting and Immunochemistry and Animal Experimentation and as recommended by funding agencies, publishers and other organizations engaged with supporting research.

DATA AVAILABILITY STATEMENT

Data are publicly available online (at https://doi.org/10.17632/v8yjx594cs.1).

ORCID

Valentina Alda Carozzi https://orcid.org/0000-0003-0963-7107
Marta Delconti https://orcid.org/0009-0002-6881-8100
Cristina Meregalli https://orcid.org/0000-0002-4281-4577

REFERENCES

Adams, J. (2004). The proteasome: A suitable antineoplastic target. *Nature Reviews. Cancer*, *4*, 349–360. https://doi.org/10.1038/nrc1361

Adams, J., & Kauffman, M. (2004). Development of the proteasome inhibitor Velcade (Bortezomib). *Cancer Investigation*, *22*, 304–311. https://doi.org/10.1081/CNV-120030218

Alé, A., Bruna, J., Herrando, M., Navarro, X., & Udina, E. (2015). Toxic effects of bortezomib on primary sensory neurons and Schwann cells of adult mice. *Neurotoxicity Research*, *27*, 430–440. https://doi.org/10.1007/s12640-014-9514-8

Alexander, S. P. H., Striessnig, J., Gibb, A. J., Mathie, A. A., Veale, E. L., Kelly, E., Peach, C. J., Armstrong, J. F., Faccenda, E., Harding, S. D., Southan, C., Davies, J. A., Aldrich, R. W., Attali, B., Baggetta, A. M., Becirovic, E., Beech, D. J., Biel, M., Bill, R. M., … Zhu, M. (2025). The Concise Guide to PHARMACOLOGY 2025/26: Ion channels. *British Journal of Pharmacology*, *182*(Suppl 1), S152–S241. https://doi.org/10.1111/bph.70231

Alexander, S. P. H., Roberts, R. E., Broughton, B. R. S., Sobey, C. G., George, C. H., Stanford, S. C., Cirino, G., Docherty, J. R., Giembycz, M. A., Hoyer, D., Insel, P. A., Izzo, A. A., Ji, Y., MacEwan, D. J., Mangum, J., Wonnacott, S., & Ahluwalia, A. (2018). Goals and practicalities of immunoblotting and immunohistochemistry: A guide for submission to the British Journal of Pharmacology. *British Journal of Pharmacology*, *175*, 407–411. https://doi.org/10.1111/bph.14112

Alsina, M., Trudel, S., Furman, R. R., Rosen, P. J., O'Connor, O. A., Comenzo, R. L., Wong, A., Kunkel, L. A., Molineaux, C. J., & Goy, A. (2012). A phase I single-agent study of twice-weekly consecutive-day dosing of the proteasome inhibitor carfilzomib in patients with relapsed or refractory multiple myeloma or lymphoma. *Clinical Cancer Research*, *18*, 4830–4840. https://doi.org/10.1158/1078-0432.CCR-11-3007

Arastu-Kapur, S., Anderl, J. L., Kraus, M., Parlati, F., Shenk, K. D., Lee, S. J., Muchamuel, T., Bennett, M. K., Driessen, C., Ball, A. J., & Kirk, C. J. (2011). Nonproteasomal targets of the proteasome inhibitors bortezomib and carfilzomib: A link to clinical adverse events. *Clinical Cancer Research*, *17*, 2734–2743. https://doi.org/10.1158/1078-0432.CCR-10-1950

Ashburner, M., Ball, C. A., Blake, J. A., Botstein, D., Butler, H., Cherry, J. M., Davis, A. P., Dolinski, K., Dwight, S. S., Eppig, J. T., Harris, M. A., Hill, D. P., Issel-Tarver, L., Kasarskis, A., Lewis, S., Matese, J. C., Richardson, J. E., Ringwald, M., Rubin, G. M., & Sherlock, G. (2000). Gene ontology: Tool for the unification of biology. *Nature Genetics*, *25*, 25–29. https://doi.org/10.1038/75556

Ballarini, E., Malacrida, A., Rodriguez-Menendez, V., Pozzi, E., Canta, A., Chiorazzi, A., Monza, L., Semperboni, S., Meregalli, C., Carozzi, V. A., Hashemi, M., Nicolini, G., Scuteri, A., Housley, S. N., Cavaletti, G., & Alberti, P. (2022). Sodium-calcium exchanger 2: A pivotal role in oxaliplatin induced peripheral neurotoxicity and axonal damage? *International Journal of Molecular Sciences*, *23*, 10063. https://doi.org/10.3390/ijms231710063

Bär, J., Popp, Y., Bucher, M., & Mikhaylova, M. (2022). Direct and indirect effects of tubulin post-translational modifications on microtubule stability: Insights and regulations. *Biochimica et Biophysica Acta, Molecular Cell Research*, *1869*, 119241. https://doi.org/10.1016/j.bbamcr.2022.119241

Betzer, C., & Jensen, P. H. (2018). Reduced cytosolic calcium as an early decisive cellular state in Parkinson's disease and synucleinopathies. *Frontiers in Neuroscience*, *12*, 819. https://doi.org/10.3389/fnins.2018.00819

Bruna, J., Udina, E., Alé, A., Vilches, J. J., Vynckier, A., Monbaliu, J., Silverman, L., & Navarro, X. (2010). Neurophysiological, histological and immunohistochemical characterization of bortezomib-induced neuropathy in mice. *Experimental Neurology*, *223*, 599–608. https://doi.org/10.1016/j.expneurol.2010.02.006

Calabrese, C., Panuzzo, C., Stanga, S., Andreani, G., Ravera, S., Maglione, A., Pironi, L., Petiti, J., Shahzad Ali, M., Scaravaglio, P., Napoli, F., Fava, C., de Gobbi, M., Frassoni, F., Saglio, G., Bracco, E., Pergolizzi, B., & Cilloni, D. (2020). Deferasirox-dependent iron chelation enhances mitochondrial dysfunction and restores p53 signaling by stabilization of p53 family members in leukemic cells. *International Journal of Molecular Sciences*, *21*, 7674. https://doi.org/10.3390/ijms21207674

Callander, N., Markovina, S., Eickhoff, J., Hutson, P., Campbell, T., Hematti, P., Go, R., Hegeman, R., Longo, W., Williams, E., Asimakopoulos, F., & Miyamoto, S. (2014). Acetyl-L-carnitine (ALCAR) for the prevention of chemotherapy-induced peripheral neuropathy in patients with relapsed or refractory multiple myeloma treated with bortezomib, doxorubicin and low-dose dexamethasone: A study from the Wisconsin Oncology Network. *Cancer Chemotherapy and Pharmacology*, *74*, 875–882. https://doi.org/10.1007/s00280-014-2550-5

Canta, A., Chiorazzi, A., Pozzi, E., Fumagalli, G., Monza, L., Meregalli, C., Carozzi, V. A., Rodriguez-Menendez, V., Oggioni, N., Näsström, J., Marmiroli, P., & Cavaletti, G. (2020). Calmangafodipir reduces sensory alterations and prevents intraepidermal nerve fibers loss in a mouse model of oxaliplatin induced peripheral neurotoxicity. *Antioxidants (Basel)*, *9*, 594. https://doi.org/10.3390/antiox9070594

Carozzi, V. A., Canta, A., & Chiorazzi, A. (2015). Chemotherapy-induced peripheral neuropathy: What do we know about mechanisms? *Neuroscience Letters*, *596*, 90–107. https://doi.org/10.1016/j.neulet.2014.10.014

Carozzi, V. A., Canta, A., Oggioni, N., Sala, B., Chiorazzi, A., Meregalli, C., Bossi, M., Marmiroli, P., & Cavaletti, G. (2010). Neurophysiological and neuropathological characterization of new murine models of chemotherapy-induced chronic peripheral neuropathies. *Experimental Neurology*, *226*, 301–309. https://doi.org/10.1016/j.expneurol.2010.09.004

Carozzi, V. A., Chiorazzi, A., Canta, A., Meregalli, C., Oggioni, N., Cavaletti, G., & Marmiroli, P. (2015). Chemotherapy-induced peripheral neurotoxicity in immune-deficient mice: New useful ready-to-use animal models. *Experimental Neurology*, *264*, 92–102. https://doi.org/10.1016/j.expneurol.2014.11.002

Carozzi, V. A., Renn, C. L., Bardini, M., Fazio, G., Chiorazzi, A., Meregalli, C., Oggioni, N., Shanks, K., Quartu, M., Serra, M. P., Sala, B., Cavaletti, G., & Dorsey, S. G. (2013). Bortezomib-induced painful peripheral neuropathy: An electrophysiological, behavioral, morphological and mechanistic study in the mouse. *PLoS ONE*, *8*, e72995. https://doi.org/10.1371/journal.pone.0072995

Cavaletti, G., Alberti, P., Argyriou, A. A., Lustberg, M., Staff, N. P., Tamburin, S., & Toxic Neuropathy Consortium of the Peripheral Nerve Society. (2019). Chemotherapy-induced peripheral neurotoxicity: A multifaceted, still unsolved issue. *Journal of the Peripheral Nervous System*, *24*(Suppl 2), S6–S12.

Cavaletti, G., Gilardini, A., Canta, A., Rigamonti, L., Rodriguez-Menendez, V., Ceresa, C., Marmiroli, P., Bossi, M., Oggioni, N., D'Incalci, M., & de Coster, R. (2007). Bortezomib-induced peripheral neurotoxicity: A neurophysiological and pathological study in the rat. *Experimental Neurology*, *204*, 317–325. https://doi.org/10.1016/j.expneurol.2006.11.010

Cavaletti, G., Tredici, G., Marmiroli, P., Petruccioli, M. G., Barajon, I., & Fabbrica, D. (1992). Morphometric study of the sensory neuron and peripheral nerve changes induced by chronic cisplatin (DDP) administration in rats. *Acta Neuropathologica*, *84*, 364–371. https://doi.org/10.1007/BF00227662

Chen, J. H., Lenihan, D. J., Phillips, S. E., Harrell, S. L., & Cornell, R. F. (2017). Cardiac events during treatment with proteasome inhibitor therapy for multiple myeloma. *Cardiooncology*, *3*, 4. https://doi.org/10.1186/s40959-017-0023-9

Cheung, L. C., de Kraa, R., Oommen, J., Chua, G. A., Singh, S., Hughes, A. M., Ferrari, E., Ford, J., Chiu, S. K., Stam, R. W., Kees, U. R., Malinge, S., & Kotecha, R. S. (2021). Preclinical evaluation of carfilzomib for infant KMT2A-rearranged acute lymphoblastic leukemia. *Frontiers in Oncology*, *11*, 631594. https://doi.org/10.3389/fonc.2021.631594

Contino, S., Suelves, N., Vrancx, C., Vadukul, D. M., Payen, V. L., Stanga, S., Bertrand, L., & Kienlen-Campard, P. (2020). Presenilin-deficient neurons and astrocytes display normal mitochondrial phenotypes. *Frontiers in Neuroscience*, *14*, 586108. https://doi.org/10.3389/fnins.2020.586108

Costa, B. A., Costa, T. A., Pak, K., Patel, A., Felix, N., Mouhieddine, T. H., & Richter, J. (2024). Comparative efficacy of carfilzomib, lenalidomide, and dexamethasone (KRd) versus bortezomib, lenalidomide, and dexamethasone (VRd) in newly-diagnosed multiple myeloma: A systematic review and meta-analysis. *American Journal of Hematology*, *99*, 1411–1414. https://doi.org/10.1002/ajh.27314

Curtis, M. J., Alexander, S. P. H., Cortese-Krott, M., Kendall, D. A., Martemyanov, K. A., Mauro, C., Panettieri, R. A. Jr., Papapetropoulos, A., Patel, H. H., Santo, E. E., Schulz, R., Stefanska, B., Stephens, G. J., Teixeira, M. M., Vergnolle, N., Wang, X., & Ferdinandy, P. (2025). Guidance on the planning and reporting of experimental design and analysis. *British Journal of Pharmacology*, *182*(7), 1413–1415. https://doi.org/10.1111/bph.17441

Cuveillier, C., Delaroche, J., Seggio, M., Gory-Fauré, S., Bosc, C., Denarier, E., Bacia, M., Schoehn, G., Mohrbach, H., Kulić, I., Andrieux, A., Arnal, I., & Delphin, C. (2020). MAP 6 is an intraluminal protein that induces neuronal microtubules to coil. *Science Advances*, *6*, eaaz4344. https://doi.org/10.1126/sciadv.aaz4344

de Nadai, A., Vajente, N., Pendin, D., & Mattarei, A. (2021). Mt-fura-2, a ratiometric mitochondria-targeted Ca2+ sensor. Determination of spectroscopic properties and Ca2+ imaging assays. *Methods in Molecular Biology*, *2275*, 187–215. https://doi.org/10.1007/978-1-0716-1262-0_12

Dehmelt, L., & Halpain, S. (2005). The MAP 2/Tau family of microtubule-associated proteins. *Genome Biology*, *6*, 204. https://doi.org/10.1186/gb-2004-6-1-204

Demo, S. D., Kirk, C. J., Aujay, M. A., Buchholz, T. J., Dajee, M., Ho, M. N., Jiang, J., Laidig, G. J., Lewis, E. R., Parlati, F., Shenk, K. D., Smyth, M. S., Sun, C. M., Vallone, M. K., Woo, T. M., Molineaux, C. J., & Bennett, M. K. (2007). Antitumor activity of PR-171, a novel irreversible inhibitor of the proteasome. *Cancer Research*, *67*, 6383–6391. https://doi.org/10.1158/0008-5472.CAN-06-4086

Doyle, T. M., & Salvemini, D. (2021). Mini-review: Mitochondrial dysfunction and chemotherapy-induced neuropathic pain. *Neuroscience Letters*, *760*, 136087. https://doi.org/10.1016/j.neulet.2021.136087

Gene Ontology Consortium, Aleksander, S. A., Balhoff, J., Carbon, S., Cherry, J. M., Drabkin, H. J., Ebert, D., Feuermann, M., Gaudet, P., Harris, N. L., Hill, D. P., Lee, R., Mi, H., Moxon, S., Mungall, C. J., Muruganugan, A., Mushayahama, T., Sternberg, P. W., Thomas, P. D., … Westerfield, M. (2023). The Gene Ontology knowledgebase in 2023. *Genetics*, *224*, iyad031. https://doi.org/10.1093/genetics/iyad031

Groen, K., van de Donk, N., Stege, C., Zweegman, S., & Nijhof, I. S. (2019). Carfilzomib for relapsed and refractory multiple myeloma. *Cancer Management and Research*, *11*, 2663–2675. https://doi.org/10.2147/CMAR.S150653

Han, S., Lee, C. Y., Besse, L., Munawar, U., Besse, A., Hainold, A. S., Nerreter, S., Vogt, C., Kurian, S., Zhou, X., Haertle, L., Waldschmidt, J., Driessen, C., Einsele, H., Rasche, L., Kuster, B., & Kortüm, K. M. (2024). Multi-omics analysis of proteasome inhibitor resistance in multiple myeloma. *Blood*, *144*, 6817. https://doi.org/10.1182/blood-2024-203352

Hristova, K., & Wimley, W. C. (2023). Determining the statistical significance of the difference between arbitrary curves: A spreadsheet

method. *PLoS ONE*, *18*, e0289619. https://doi.org/10.1371/journal.pone.0289619

Hrstka, S. C. L., Ankam, S., Agac, B., Klein, J. P., Moore, R. A., Narapureddy, B., Schneider, I., Hrstka, R. F., Dasari, S., & Staff, N. P. (2021). Proteomic analysis of human iPSC-derived sensory neurons implicates cell stress and microtubule dynamics dysfunction in bortezomib-induced peripheral neurotoxicity. *Experimental Neurology*, *335*, 113520. https://doi.org/10.1016/j.expneurol.2020.113520

Janes, K., Doyle, T., Bryant, L., Esposito, E., Cuzzocrea, S., Ryerse, J., Bennett, G. J., & Salvemini, D. (2013). Bioenergetic deficits in peripheral nerve sensory axons during chemotherapy-induced neuropathic pain resulting from peroxynitrite-mediated post-translational nitration of mitochondrial superoxide dismutase. *Pain*, *154*, 2432–2440. https://doi.org/10.1016/j.pain.2013.07.032

Jannuzzi, A. T., Arslan, S., Yilmaz, A. M., Sari, G., Beklen, H., Méndez, L., Fedorova, M., Arga, K. Y., Karademir Yilmaz, B., & Alpertunga, B. (2020). Higher proteotoxic stress rather than mitochondrial damage is involved in higher neurotoxicity of bortezomib compared to carfilzomib. *Redox Biology*, *32*, 101502. https://doi.org/10.1016/j.redox.2020.101502

Karademir, B., Sari, G., Jannuzzi, A. T., Musunuri, S., Wicher, G., Grune, T., Mi, J., Hacioglu-Bay, H., Forsberg-Nilsson, K., Bergquist, J., & Jung, T. (2018). Proteomic approach for understanding milder neurotoxicity of Carfilzomib against Bortezomib. *Scientific Reports*, *8*, 16318. https://doi.org/10.1038/s41598-018-34507-3

Kriz, J., Meier, J., Julien, J. P., & Padjen, A. L. (2000). Altered ionic conductances in axons of transgenic mouse expressing the human neurofilament heavy gene: A mouse model of amyotrophic lateral sclerosis. *Experimental Neurology*, *163*, 414–421. https://doi.org/10.1006/exnr.2000.7378

Kuhn, D. J., Chen, Q., Voorhees, P. M., Strader, J. S., Shenk, K. D., Sun, C. M., Demo, S. D., Bennett, M. K., van Leeuwen, F. W. B., Chanan-Khan, A. A., & Orlowski, R. Z. (2007). Potent activity of carfilzomib, a novel, irreversible inhibitor of the ubiquitin-proteasome pathway, against preclinical models of multiple myeloma. *Blood*, *110*, 3281–3290. https://doi.org/10.1182/blood-2007-01-065888

Kumar, S. K., Jacobus, S. J., Cohen, A. D., Weiss, M., Callander, N., Singh, A. K., Parker, T. L., Menter, A., Yang, X., Parsons, B., Kumar, P., Kapoor, P., Rosenberg, A., Zonder, J. A., Faber, E. Jr., Lonial, S., Anderson, K. C., Richardson, P. G., Orlowski, R. Z., … Rajkumar, S. V. (2020). Carfilzomib or bortezomib in combination with lenalidomide and dexamethasone for patients with newly diagnosed multiple myeloma without intention for immediate autologous stem-cell transplantation (ENDURANCE): A multicentre, open-label, phase 3, randomised, controlled trial. *The Lancet Oncology*, *21*, 1317–1330. https://doi.org/10.1016/S1470-2045(20)30452-6

Landowski, T. H., Megli, C. J., Nullmeyer, K. D., Lynch, R. M., & Dorr, R. T. (2005). Mitochondrial-mediated disregulation of Ca2+ is a critical determinant of Velcade (PS-341/bortezomib) cytotoxicity in myeloma cell lines. *Cancer Research*, *65*, 3828–3836. https://doi.org/10.1158/0008-5472.CAN-04-3684

Li, T., Timmins, H. C., King, T., Kiernan, M. C., Goldstein, D., & Park, S. B. (2020). Characteristics and risk factors of bortezomib induced peripheral neuropathy: A systematic review of phase III trials. *Hematological Oncology*, *38*, 229–243. https://doi.org/10.1002/hon.2706

Li, Y., Drabison, T., Nepal, M., Ho, R. H., Leblanc, A. F., Gibson, A. A., Jin, Y., Yang, W., Huang, K. M., Uddin, M. E., Chen, M., DiGiacomo, D. F., Chen, X., Razzaq, S., Tonniges, J. R., McTigue, D. M., Mims, A. S., Lustberg, M. B., Wang, Y., … Hu, S. (2023). Targeting a xenobiotic transporter to ameliorate vincristine-induced sensory neuropathy. *JCI Insight*, *8*, e164646. https://doi.org/10.1172/jci.insight.164646

Lilley, E., Stanford, S. C., Kendall, D. E., Alexander, S. P. H., Cirino, G., Docherty, J. R., George, C. H., Insel, P. A., Izzo, A. A., Ji, Y., Panettieri, R. A., Sobey, C. G., Stefanska, B., Stephens, G., Teixeira, M., & Ahluwalia, A. (2020). ARRIVE 2.0 and the British Journal of Pharmacology: Updated guidance for 2020. *British Journal of Pharmacology*, *177*, 3611–3616. https://doi.org/10.1111/bph.15178

Ludwig, K. R., Schroll, M. M., & Hummon, A. B. (2018). Comparison of in-solution, FASP, and S-trap based digestion methods for bottom-up proteomic studies. *Journal of Proteome Research*, *17*, 2480–2490. https://doi.org/10.1021/acs.jproteome.8b00235

Maharjan, S., Oku, M., Tsuda, M., Hoseki, J., & Sakai, Y. (2014). Mitochondrial impairment triggers cytosolic oxidative stress and cell death following proteasome inhibition. *Scientific Reports*, *4*, 5896. https://doi.org/10.1038/srep05896

Malacrida, A., Semperboni, S., di Domizio, A., Palmioli, A., Broggi, L., Airoldi, C., Meregalli, C., Cavaletti, G., & Nicolini, G. (2021). Tubulin binding potentially clears up bortezomib and carfilzomib differential neurotoxic effect. *Scientific Reports*, *11*, 10523. https://doi.org/10.1038/s41598-021-89856-3

Martin, T. G. (2013). Peripheral neuropathy experience in patients with relapsed and/or refractory multiple myeloma treated with carfilzomib. *Oncology (Williston Park)*, *27*(Suppl 3), 4–10.

Meregalli, C., Canta, A., Carozzi, V. A., Chiorazzi, A., Oggioni, N., Gilardini, A., Ceresa, C., Avezza, F., Crippa, L., Marmiroli, P., & Cavaletti, G. (2010). Bortezomib-induced painful neuropathy in rats: A behavioral, neurophysiological and pathological study in rats. *European Journal of Pain*, *14*, 343–350. https://doi.org/10.1016/j.ejpain.2009.07.001

Meregalli, C., Carozzi, V. A., Sala, B., Chiorazzi, A., Canta, A., Oggioni, N., Rodriguez-Menendez, V., Ballarini, E., Ceresa, C., Nicolini, G., Crippa, L., Orciani, M., Cavaletti, G., & Marmiroli, P. (2015). Bortezomib-induced peripheral neurotoxicity in human multiple myeloma-bearing mice. *Journal of Biological Regulators and Homeostatic Agents*, *29*, 115–124.

Meregalli, C., Chiorazzi, A., Carozzi, V. A., Canta, A., Sala, B., Colombo, M., Oggioni, N., Ceresa, C., Foudah, D., la Russa, F., Miloso, M., Nicolini, G., Marmiroli, P., Bennett, D. L. H., & Cavaletti, G. (2014). Evaluation of tubulin polymerization and chronic inhibition of proteasome as citotoxicity mechanisms in bortezomib-induced peripheral neuropathy. *Cell Cycle*, *13*, 612–621. https://doi.org/10.4161/cc.27476

Meregalli, C., Maricich, Y., Cavaletti, G., Canta, A., Carozzi, V. A., Chiorazzi, A., Newbold, E., Marmiroli, P., Ceresa, C., Diani, A., Papapetropoulos, S., & Lee, M. S. (2021). Reversal of bortezomib-induced neurotoxicity by suvecaltamide, a selective T-type Ca-channel modulator, in preclinical models. *Cancers (Basel)*, *13*, 5013. https://doi.org/10.3390/cancers13195013

Meregalli, C., Marjanovic, I., Scali, C., Monza, L., Spinoni, N., Galliani, C., Brivio, R., Chiorazzi, A., Ballarini, E., Rodriguez-Menendez, V., Carozzi, V. A., Alberti, P., Fumagalli, G., Pozzi, E., Canta, A., Quartu, M., Briani, C., Oggioni, N., Marmiroli, P., & Cavaletti, G. (2018). High-dose intravenous immunoglobulins reduce nerve macrophage infiltration and the severity of bortezomib-induced peripheral neurotoxicity in rats. *Journal of Neuroinflammation*, *15*, 232. https://doi.org/10.1186/s12974-018-1270-x

Monza, L., Fumagalli, G., Chiorazzi, A., & Alberti, P. (2021). Addressing the need of a translational approach in peripheral neuropathy research: Morphology meets function. *Brain Sciences*, *11*, 139. https://doi.org/10.3390/brainsci11020139

Morcillo, P., Kabra, K., Velasco, K., Cordero, H., Jennings, S., Yun, T. D., Larrea, D., Akman, H. O., & Schon, E. A. (2024). Aberrant ER-mitochondria communication is a common pathomechanism in mitochondrial disease. *Cell Death & Disease*, *15*, 405. https://doi.org/10.1038/s41419-024-06781-9

O'Connor, O. A., Stewart, A. K., Vallone, M., Molineaux, C. J., Kunkel, L. A., Gerecitano, J. F., & Orlowski, R. Z. (2009). A phase 1 dose escalation study of the safety and pharmacokinetics of the novel proteasome

inhibitor carfilzomib (PR-171) in patients with hematologic malignancies. *Clinical Cancer Research*, *15*, 7085–7091. https://doi.org/10.1158/1078-0432.CCR-09-0822

Panuzzo, C., Pironi, L., Maglione, A., Rocco, S., Stanga, S., Riganti, C., Kopecka, J., Ali, M. S., Pergolizzi, B., Bracco, E., & Cilloni, D. (2023). mTORC2 is activated under hypoxia and could support chronic myeloid leukemia stem cells. *International Journal of Molecular Sciences*, *24*, 1234. https://doi.org/10.3390/ijms24021234

Pendin, D., Norante, R., de Nadai, A., Gherardi, G., Vajente, N., Basso, E., Kaludercic, N., Mammucari, C., Paradisi, C., Pozzan, T., & Mattarei, A. (2019). A synthetic fluorescent mitochondria-targeted sensor for ratiometric imaging of calcium in live cells. *Angewandte Chemie (International Ed. in English)*, *58*, 9917–9922. https://doi.org/10.1002/anie.201902272

Peng, L., Ye, X., Zhou, Y., Zhang, J., & Zhao, Q. (2015). Meta-analysis of incidence and risk of peripheral neuropathy associated with intravenous bortezomib. *Support Care Cancer*, *23*, 2813–2824. https://doi.org/10.1007/s00520-015-2648-2

Percie du Sert, N., Hurst, V., Ahluwalia, A., Alam, S., Avey, M. T., Baker, M., Browne, W. J., Clark, A., Cuthill, I. C., Dirnagl, U., Emerson, M., Garner, P., Holgate, S. T., Howells, D. W., Karp, N. A., Lazic, S. E., Lidster, K., MacCallum, C. J., Macleod, M., … Würbel, H. (2020). The ARRIVE guidelines 2.0: Updated guidelines for reporting animal research. *PLoS Biology*, *18*(7), e3000410. https://doi.org/10.1371/journal.pbio.3000410

Pero, M. E., Meregalli, C., Qu, X., Shin, G. J. E., Kumar, A., Shorey, M., Rolls, M. M., Tanji, K., Brannagan, T. H., Alberti, P., Fumagalli, G., Monza, L., Grueber, W. B., Cavaletti, G., & Bartolini, F. (2021). Pathogenic role of delta 2 tubulin in bortezomib-induced peripheral neuropathy. *Proceedings of the National Academy of Sciences of the United States of America*, *118*, e2012685118. https://doi.org/10.1073/pnas.2012685118

Porras-Yakushi, T. R., Reitsma, J. M., Sweredoski, M. J., Deshaies, R. J., & Hess, S. (2021). In-depth proteomic analysis of proteasome inhibitors bortezomib, carfilzomib and MG132 reveals that mortality factor 4-like 1 (MORF4L1) protein ubiquitylation is negatively impacted. *Journal of Proteomics*, *241*, 104197. https://doi.org/10.1016/j.jprot.2021.104197

Poruchynsky, M. S., Sackett, D. L., Robey, R. W., Ward, Y., Annunziata, C., & Fojo, T. (2008). Proteasome inhibitors increase tubulin polymerization and stabilization in tissue culture cells: A possible mechanism contributing to peripheral neuropathy and cellular toxicity following proteasome inhibition. *Cell Cycle*, *7*, 940–949. https://doi.org/10.4161/cc.7.7.5625

Pozzi, E., Fumagalli, G., Chiorazzi, A., Canta, A., Meregalli, C., Monza, L., Carozzi, V. A., Oggioni, N., Rodriguez-Menendez, V., Cavaletti, G., & Marmiroli, P. (2020). The relevance of multimodal assessment in experimental oxaliplatin-induced peripheral neurotoxicity. *Experimental Neurology*, *334*, 113458. https://doi.org/10.1016/j.expneurol.2020.113458

Previtali, P., Pagani, L., Risca, G., Capitoli, G., Bossi, E., Oliveira, G., Piga, I., Radice, A., Trezzi, B., Sinico, R. A., Magni, F., & Chinello, C. (2023). Towards the definition of the molecular hallmarks of idiopathic membranous nephropathy in serum proteome: A DIA-PASEF approach. *International Journal of Molecular Sciences*, *24*, 11756. https://doi.org/10.3390/ijms241411756

Robinson, C. R., Zhang, H., & Dougherty, P. M. (2014). Astrocytes, but not microglia, are activated in oxaliplatin and bortezomib-induced peripheral neuropathy in the rat. *Neuroscience*, *274*, 308–317. https://doi.org/10.1016/j.neuroscience.2014.05.051

Roy, A., Kish, J. K., Bloudek, L., Siegel, D. S., Jagannath, S., Globe, D., Kuriakose, E. T., & Migliaccio-Walle, K. (2015). Estimating the costs of therapy in patients with relapsed and/or refractory multiple myeloma: A model framework. *American Health & Drug Benefits*, *8*, 204–215.

Schwarz, T. L. (2013). Mitochondrial trafficking in neurons. *Cold Spring Harbor Perspectives in Biology*, *5*, a011304. https://doi.org/10.1101/cshperspect.a011304

Shah, C., Bishnoi, R., Wang, Y., Zou, F., Bejjanki, H., Master, S., & Moreb, J. S. (2018). Efficacy and safety of carfilzomib in relapsed and/-or refractory multiple myeloma: Systematic review and meta-analysis of 14 trials. *Oncotarget*, *9*, 23704–23717. https://doi.org/10.18632/oncotarget.25281

Sheng, Z., Li, G., Li, B., Liu, Y., & Wang, L. (2017). Carfilzomib-containing combinations as frontline therapy for multiple myeloma: A meta-analysis of 13 trials. *European Journal of Haematology*, *98*, 601–607. https://doi.org/10.1111/ejh.12877

Sheng, Z.-H. (2017). The interplay of axonal energy homeostasis and mitochondrial trafficking and anchoring. *Trends in Cell Biology*, *27*, 403–416. https://doi.org/10.1016/j.tcb.2017.01.005

Shin, G. J., Pero, M. E., Hammond, L. A., Burgos, A., Kumar, A., Galindo, S. E., Tanguy, L., Bartolini, F., & Grueber, W. B. (2021). Integrins protect sensory neurons in models of paclitaxel-induced peripheral sensory neuropathy. *Proceedings of the National Academy of Sciences of the United States of America*, *118*(15), e2006050118. https://doi.org/10.1073/pnas.2006050118

Siegel, D., Martin, T., Nooka, A., Harvey, R. D., Vij, R., Niesvizky, R., Badros, A. Z., Jagannath, S., McCulloch, L., Rajangam, K., & Lonial, S. (2013). Integrated safety profile of single-agent carfilzomib: Experience from 526 patients enrolled in 4 Phase II clinical studies. *Haematologica*, *98*, 1753–1761. https://doi.org/10.3324/haematol.2013.089334

Siegel, D. S., Martin, T., Wang, M., Vij, R., Jakubowiak, A. J., Lonial, S., Trudel, S., Kukreti, V., Bahlis, N., Alsina, M., Chanan-Khan, A., Buadi, F., Reu, F. J., Somlo, G., Zonder, J., Song, K., Stewart, A. K., Stadtmauer, E., Kunkel, L., … Jagannath, S. (2012). A phase 2 study of single-agent carfilzomib (PX-171-003-A1) in patients with relapsed and refractory multiple myeloma. *Blood*, *120*, 2817–2825. https://doi.org/10.1182/blood-2012-05-425934

Smith, J. A., Slusher, B. S., Wozniak, K. M., Farah, M. H., Smiyun, G., Wilson, L., Feinstein, S., & Jordan, M. A. (2016). Structural basis for induction of peripheral neuropathy by microtubule-targeting cancer drugs. *Cancer Research*, *76*, 5115–5123. https://doi.org/10.1158/0008-5472.CAN-15-3116

Snavely, A. R., Heo, K., Petrova, V., Ho, T. S. Y., Huang, X., Hermawan, C., Kagan, R., Deng, T., Singeç, I., Chen, L., Barret, L. B., & Woolf, C. J. (2022). Bortezomib-induced neurotoxicity in human neurons is the consequence of nicotinamide adenine dinucleotide depletion. *Disease Models & Mechanisms*, *15*, dmm049358. https://doi.org/10.1242/dmm.049358

Staff, N. P., Podratz, J. L., Grassner, L., Bader, M., Paz, J., Knight, A. M., Loprinzi, C. L., Trushina, E., & Windebank, A. J. (2013). Bortezomib alters microtubule polymerization and axonal transport in rat dorsal root ganglion neurons. *Neurotoxicology*, *39*, 124–131. https://doi.org/10.1016/j.neuro.2013.09.001

Stanga, S., Caretto, A., Boido, M., & Vercelli, A. (2020). Mitochondrial dysfunctions: A red thread across neurodegenerative diseases. *International Journal of Molecular Sciences*, *21*, 3719. https://doi.org/10.3390/ijms21103719

Starobova, H., & Vetter, I. (2017). Pathophysiology of chemotherapy-induced peripheral neuropathy. *Frontiers in Molecular Neuroscience*, *10*, 174. https://doi.org/10.3389/fnmol.2017.00174

Strifler, S., & Knop, S. (2018). The role of carfilzomib in treatment of newly diagnosed multiple myeloma. *Future Oncology*, *14*, 3123–3134. https://doi.org/10.2217/fon-2018-0040

Szklarczyk, D., Kirsch, R., Koutrouli, M., Nastou, K., Mehryary, F., Hachilif, R., Gable, A. L., Fang, T., Doncheva, N. T., Pyysalo, S., Bork, P., Jensen, L. J., & von Mering, C. (2023). The STRING database in 2023: Protein-protein association networks and functional

enrichment analyses for any sequenced genome of interest. *Nucleic Acids Research*, *51*, D638–D646. https://doi.org/10.1093/nar/gkac1000

Tábara, L.-C., Segawa, M., & Prudent, J. (2025). Molecular mechanisms of mitochondrial dynamics. *Nature Reviews. Molecular Cell Biology*, *26*, 123–146. https://doi.org/10.1038/s41580-024-00785-1

Tan, C. R., Derkach, A., Nemirovsky, D., Ciardiello, A., Diamond, B., Hultcrantz, M., Hassoun, H., Mailankody, S., Shah, U., Maclachlan, K., Patel, D., Lahoud, O. B., Landau, H. J., Chung, D. J., Shah, G. L., Scordo, M., Giralt, S. A., Lesokhin, A., Usmani, S. Z., … Korde, N. (2023). Bortezomib, lenalidomide and dexamethasone (VRd) vs carfilzomib, lenalidomide and dexamethasone (KRd) as induction therapy in newly diagnosed multiple myeloma. *Blood Cancer Journal*, *13*, 112. https://doi.org/10.1038/s41408-023-00882-y

Thomas, P. D., Ebert, D., Muruganujan, A., Mushayahama, T., Albou, L. P., & Mi, H. (2022). PANTHER: Making genome-scale phylogenetics accessible to all. *Protein Science*, *31*, 8–22. https://doi.org/10.1002/pro.4218

Tomita, S., Sekiguchi, F., Deguchi, T., Miyazaki, T., Ikeda, Y., Tsubota, M., Yoshida, S., Nguyen, H. D., Okada, T., Toyooka, N., & Kawabata, A. (2019). Critical role of Cav3.2 T-type calcium channels in the peripheral neuropathy induced by bortezomib, a proteasome-inhibiting chemotherapeutic agent, in mice. *Toxicology*, *413*, 33–39. https://doi.org/10.1016/j.tox.2018.12.003

Valente, A. J., Maddalena, L. A., Robb, E. L., Moradi, F., & Stuart, J. A. (2017). A simple ImageJ macro tool for analyzing mitochondrial network morphology in mammalian cell culture. *Acta Histochemica*, *119*, 315–326. https://doi.org/10.1016/j.acthis.2017.03.001

Velasco, R., Alberti, P., Bruna, J., Psimaras, D., & Argyriou, A. A. (2019). Bortezomib and other proteosome inhibitors-induced peripheral neurotoxicity: From pathogenesis to treatment. *Journal of the Peripheral Nervous System*, *24*(Suppl 2), S52–S62. https://doi.org/10.1111/jns.12338

Villalón, E., Barry, D. M., Byers, N., Frizzi, K., Jones, M. R., Landayan, D. S., Dale, J. M., Downer, N. L., Calcutt, N. A., & Garcia, M. L. (2018). Internode length is reduced during myelination and remyelination by neurofilament medium phosphorylation in motor axons. *Experimental Neurology*, *306*, 158–168. https://doi.org/10.1016/j.expneurol.2018.05.009

Wen, D., Cao, S., & Feng, Y. (2023). Recent advances in the treatment and prevention of peripheral neuropathy after multiple myeloma treatment. *Ibrain*, *9*, 421–430. https://doi.org/10.1002/ibra.12132

White, D., Abdulla, M., Park, S. B., Goldstein, D., Moalem-Taylor, G., & Lees, J. G. (2023). Targeting translation: A review of preclinical animal models in the development of treatments for chemotherapy-induced peripheral neuropathy. *Journal of the Peripheral Nervous System*, *28*, 179–190. https://doi.org/10.1111/jns.12544

Wolf, J. L., Vij, R., Lonial, S., Wang, M., Jagannath, S., Singhal, S., Le, M. H., Kirk, C., Arastu-Kapur, S., Siegel, D. S., & The Multiple Myeloma Research Consortium. (2010). Neurotoxic and peripheral neuropathic effects in preclinical and clinical studies of carfilzomib (CFZ), a novel proteasome inhibitor (PI). *JCO*, *28*, 8135. https://doi.org/10.1200/jco.2010.28.15_suppl.8135

Wu, D., Wang, F., Yang, X., Yang, B., Chen, J., Cheng, J., Wei, B., Yuan, X., Tian, T., Liu, Z., He, Z., Liu, Y., & Li, Y. (2025). Efficacy of maintenance or consolidation therapy for multiple myeloma based on proteasome inhibitors: a meta-analysis. *Discover Oncology*, *16*, 519. https://doi.org/10.1007/s12672-025-02304-w

Xie, C., Wei, M., Yang, F., Liu, Q., Wu, F., & Huang, J. (2022). Efficacy and toxicity of carfilzomib- or bortezomib-based regimens for treatment of transplant-ineligible patients with newly diagnosed multiple myeloma: A meta-analysis. *Medicine (Baltimore)*, *101*, e30715. https://doi.org/10.1097/MD.0000000000030715

Yamamoto, S., Kawashiri, T., Higuchi, H., Tsutsumi, K., Ushio, S., Kaname, T., Shirahama, M., & Egashira, N. (2015). Behavioral and pharmacological characteristics of bortezomib-induced peripheral neuropathy in rats. *Journal of Pharmacological Sciences*, *129*, 43–50. https://doi.org/10.1016/j.jphs.2015.08.006

Yan, W., Wu, Z., Zhang, Y., Hong, D., Dong, X., Liu, L., Rao, Y., Huang, L., Zhang, X., & Wu, J. (2021). The molecular and cellular insight into the toxicology of bortezomib-induced peripheral neuropathy. *Biomedicine & Pharmacotherapy*, *142*, 112068. https://doi.org/10.1016/j.biopha.2021.112068

Yang, X.-X., Yao, G., Yang, Y., Han, Y., Yang, L., & Zhang, Y. (2024). Meta-analysis of effectiveness and safety of proteasome inhibitor-dependent maintenance treatment for multiple myeloma a systematic review. *Heliyon*, *10*, e36311. https://doi.org/10.1016/j.heliyon.2024.e36311

Yang, Y., Zhao, B., Lan, H., Sun, J., & Wei, G. (2024). Bortezomib-induced peripheral neuropathy: Clinical features, molecular basis, and therapeutic approach. *Critical Reviews in Oncology/Hematology*, *197*, 104353. https://doi.org/10.1016/j.critrevonc.2024.104353

Yee, A. J. (2021). The role of carfilzomib in relapsed/refractory multiple myeloma. *Therapeutic Advances in Hematology*, *12*, 2040620 7211019612. https://doi.org/10.1177/20406207211019612

Zheng, H., Xiao, W. H., & Bennett, G. J. (2012). Mitotoxicity and bortezomib-induced chronic painful peripheral neuropathy. *Experimental Neurology*, *238*, 225–234. https://doi.org/10.1016/j.expneurol.2012.08.023

SUPPORTING INFORMATION

Additional supporting information can be found online in the Supporting Information section at the end of this article.

How to cite this article: Iseppon, F., Malacrida, A., Chiorazzi, A., Canta, A., Alberti, P., Carozzi, V. A., Pozzi, E., Rodriguez-Menendez, V., Cherchi, L., Fabbro, V., Pagani, L., Tonelli, E., Tapella, L., Mattarei, A., Palermo, S., Cartelli, D., Mauri, M., Scimia, N., Stanga, S., … Meregalli, C. (2026). Shared and specific molecular mechanisms of proteasome inhibitors in chemotherapy-induced peripheral neurotoxicity. *British Journal of Pharmacology*, 1–28. https://doi.org/10.1111/bph.70501